JOURNAL OF PETROLOGY | VOLUME 49 | NUMBER 12 | PAGES 2187–2220 | 2008 | doi:10.1093/petrology/egn065

Juxtaposition of Melt Impregnation and High-Temperature Shear Zones in the Upper Mantle; Field and Petrological Constraints from the Lanzo Peridotite (Northern Italy)

MARY-ALIX KACZMAREK[1]* AND OTHMAR MÜNTENER[2]

[1]INSTITUTE OF GEOLOGY, UNIVERSITY OF NEUCHÂTEL, RUE EMILE ARGAND, 2007 NEUCHÂTEL, SWITZERLAND
[2]INSTITUTE OF MINERALOGY AND GEOCHEMISTRY, UNIVERSITY OF LAUSANNE, ANTHROPOLE, CH-1015 LAUSANNE, SWITZERLAND

RECEIVED NOVEMBER 29, 2007; ACCEPTED NOVEMBER 13, 2008
ADVANCE ACCESS PUBLICATION DECEMBER 16, 2008

Results of a field and microstructural study between the northern and the central bodies of the Lanzo plagioclase peridotite massif (NW Italy) indicate that the spatial distribution of deformation is asymmetric across kilometre-scale mantle shear zones. The south-western part of the shear zone (footwall) shows a gradually increasing degree of deformation from porphyroclastic peridotites to mylonite, whereas the northeastern part (hanging wall) quickly grades into weakly deformed peridotites. Discordant gabbroic and basaltic dykes are asymmetrically distributed and far more abundant in the footwall of the shear zone. The porphyroclastic peridotite displays porphyroclastic zones and domains of igneous crystallization whereas mylonites are characterized by elongated porphyroclasts, embedded between fine-grained, polycrystalline bands of olivine, plagioclase, clinopyroxene, orthopyroxene, spinel, rare titanian pargasite, and domains of recrystallized olivine. Two types of melt impregnation textures have been found: (1) clinopyroxene porphyroclasts incongruently reacted with migrating melt to form orthopyroxene + plagioclase; (2) olivine porphyroclasts are partially replaced by interstitial orthopyroxene. The melt–rock reaction textures tend to disappear in the mylonites, indicating that deformation in the mylonite continued under subsolidus conditions. The pyroxene chemistry is correlated with grain size. High-Al pyroxene cores indicate high temperatures (1100–1030°C), whereas low-Al neoblasts display lower final equilibration temperatures (~860°C). The spinel Cr-number [molar Cr/(Cr + Al)] and TiO_2 concentrations show extreme variability covering almost the entire range known from abyssal peridotites. The spinel compositions of porphyroclastic peridotites from the central body are more variable than spinel from mylonite, mylonite with ultra-mylonite bands, and porphyroclastic rocks of the northern body. The spinel compositions probably indicate disequilibrium and would favour rapid cooling, and a faster exhumation of the central peridotite body, relative to the northern one. Our results indicate that melt migration and high-temperature deformation are juxtaposed both in time and space. Melt–rock reaction may have caused grain-size reduction, which in turn led to localization of deformation. It is likely that melt-lubricated, actively deforming peridotites acted as melt focusing zones, with permeabilities higher than the surrounding, less deformed peridotites. Later, under subsolidus conditions, pinning in polycrystalline bands in the mylonites inhibited substantial grain growth and led to permanent weak zones in the upper mantle peridotite, with a permeability that is lower than in the weakly deformed peridotites. Such an inversion in permeability might explain why actively deforming, fine-grained peridotite mylonite acted as a permeability barrier and why ascending mafic melts might terminate and crystallize as gabbros along actively deforming shear zones. Melt-lubricated mantle shear zones provide a mechanism for explaining the discontinuous distribution of gabbros in ocean–continent transition zones, oceanic core complexes and ultraslow-spreading ridges.

KEY WORDS: *plagioclase peridotite; Lanzo massif; mantle shear zones; permeability barriers; melt impregnation; reactive fractionation*

*Corresponding author. Present address: Géosciences Montpellier, UMR 5243–CC60, Université Montpellier 2, Place E. Bataillon, F-34095 Montpellier cédex 5, France. Telephone: +33 (0) 4 67 14 36 43. Fax: +33 (0) 4 67 14 36 42. E-mail: Mary-Alix.kaczmarek@gm.univ-montp2.fr

INTRODUCTION

Peridotite mylonites in the oceanic lithosphere are widely considered as important features for exhumation of mantle rocks to the ocean floor in ocean–continent transition zones and at mid-ocean ridges, in particular in (ultra-)slow-spreading ridges and along transform faults (Cannat, 1993; Jaroslow *et al.*, 1996; Tucholke *et al.*, 2001). Forsterite-rich olivine dominates the upper mantle composition and, being a relatively weak mineral, controls mantle rheology (Drury *et al.*, 1990; Drury & Fitz Gerald, 1998). Peridotite mylonite may control the strength of the mantle lithosphere (Vissers *et al.*, 1995, 1997) and therefore play a crucial role in lithosphere-scale deformation processes such as continental rifting or oceanic core complex formation. The processes that could induce substantial weakening of mantle peridotite and localize deformation result from the combined effects of thermal reaction and a change in the dominant reaction mechanism (Drury *et al.*, 1990; Drury, 2005). The presence of small amounts of interstitial melt is known to lower the resistance to stress in solid-state flow (Hirth & Kohlstedt, 1995) and to promote recrystallization and grain growth. Small melt fractions have an important influence on the physical properties of rocks (such as seismic velocities) that are sensitive to the grain-scale distribution of melt. In actively deforming polyphase rocks such as upper mantle peridotite grain growth is often inhibited by grain boundary pinning (Olgaard & Evans, 1988) and a stable grain size develops depending on the grain size and volume fraction of the phases other than olivine. Permanent grain-size reduction might occur in melt- and H_2O-free peridotites (Warren & Hirth, 2006), but also in peridotites that were affected by melt–rock reaction (e.g. Dijkstra *et al.*, 2002). Dijkstra *et al.* concluded that grain-size reduction by melt–rock reaction, combined with mechanical mixing of mineral phases, provides an important mechanism for weakening and strain localization in mantle rocks.

To explore the effects of deformation on melt migration processes in the upper mantle we performed a detailed field and mineral chemistry study on deformed plagioclase peridotites from the Lanzo peridotite. This mantle shear zone was originally interpreted as a zone that separates a mantle diapir (Lanzo South Central) from the surrounding peridotite (Boudier & Nicolas, 1972; Boudier, 1978). More recent studies have shown the Lanzo peridotite to have originally been lithospheric mantle that underwent significant modification by melt–rock reaction processes (e.g. Müntener & Piccardo, 2003; Müntener *et al.*, 2005; Piccardo *et al.*, 2007), although the relationship of melt migration features to deformation is poorly constrained.

The complexity of this study arises from the fact that the rocks record transient processes in space and time, such as deformation and melt migration as a result of the body's migration down a temperature gradient. Therefore, the kinetics of all processes are changing internally and relative to each other through time. In this paper we provide a detailed study of the field, microtextural, thermometric and mineral chemistry data to better understand how peridotite records deformation and melt interaction during cooling. We present a detailed structural map showing the different groups of peridotite microstructures; these display a gradual increase in deformation on a kilometre scale approaching a zone of mylonitic rocks that separates the central from the porphyroclastic northern Lanzo peridotite body. We discuss the effects of variable deformation with respect to mineral composition, in particular spinel. We propose that the disequilibrium mineral compositions recorded in the porphyroclastic peridotites indicate melt infiltration in a thermal boundary layer followed by rapid cooling and exhumation of the peridotite in the footwall of a major mantle shear zone. The strongly deformed (i.e. finer grained) shear zone rocks are, in contrast, compositionally much more homogeneous. We discuss the role of mantle shear zones with respect to melt migration, and argue that melt-lubricated shear zones might act as a melt focusing mechanism for migrating liquids in the upper mantle.

GEOLOGICAL SETTING

The Lanzo massif is located in Northern Italy, NW of Torino, and forms part of the high-pressure metamorphic belt of the internal Western Alps. To the west the massif is in contact with the Piemontese ophiolites and to the east it is covered by late Cenozoic sediments (Fig. 1). Earlier studies divided the Lanzo massif into three parts: a northern (5 km^2), a central (~90 km^2) and a southern body (55 km^2), each separated by partially serpentinized mylonitic shear zones (Nicolas *et al.*, 1972; Figs 1 and 2). The entire massif is dominated by plagioclase peridotite and was mapped structurally by Boudier (1978), who presented maps showing the regional distribution of pyroxenite layering, high-temperature foliation and gabbroic dykes. In the northern and central parts of the massif, pyroxenites and high-temperature foliation are mostly discordant whereas in the southern body pyroxenite layering and high-temperature foliation are concordant (Fig. 1). The pyroxenite layering is locally folded with the development of an axial planar foliation, presumably reflecting an old, lithospheric history of the massif (Boudier, 1978). Previous geochemical data have defined two main domains: (1) the northern, fertile lherzolitic body, which has been considered to represent a fragment of subcontinental lithosphere that became isolated from the convective mantle some 400–700 Myr ago (Bodinier *et al.*, 1991); (2) the southern body, which displays a more refractory composition (Bodinier, 1988; Bodinier *et al.*, 1991) and has been interpreted as an asthenospheric diapir that rose from the garnet stability field, and was emplaced in the

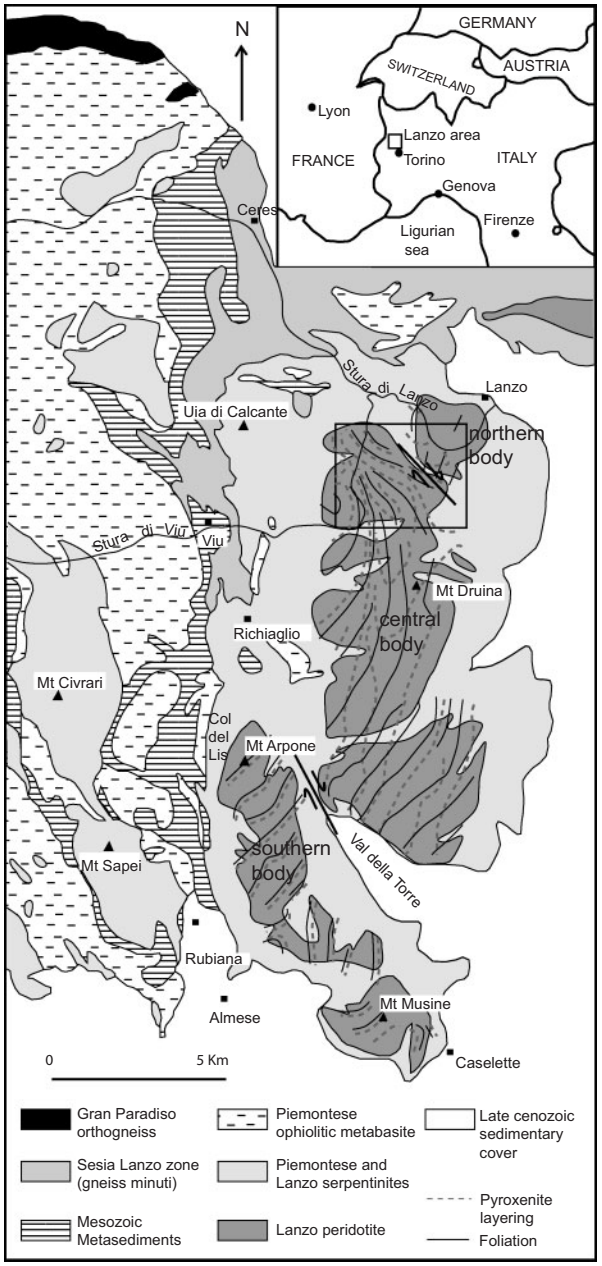

Fig. 1. Tectonic map of the Lanzo massif, modified after Boudier & Nicolas (1972), Boudier (1978) and Pognante (1989). The box corresponds to the detailed study area shown in Fig. 2.

early Mesozoic, during the opening of the Ligurian Tethys. The Lanzo peridotite has an overall fertile composition with respect to primitive mantle abundances, with calculated melt extraction of about 6% in the northern body and 6–12% in the southern body (Bodinier, 1988). The extracted melts have a transitional mid-ocean ridge basalt (T-MORB) composition in the north, and a T- to normal (N-)MORB composition in the central and southern part, respectively (Bodinier, 1988). The Lanzo massif shows evidence of melt formation and melt extraction (Boudier & Nicolas, 1972; Boudier, 1978; Nicolas, 1986) such as plagioclase–pyroxene clusters, plagioclase lenses and dunites. More recent studies emphasize the role of 'asthenospherization' of a previous lithospheric mantle domain (Müntener & Piccardo, 2003; Piccardo *et al.*, 2004; Müntener *et al.*, 2005). The massif contains numerous igneous rocks ranging from troctolites and olivine gabbros to oxide gabbros and porphyritic basaltic dykes (Boudier & Nicolas, 1972; Boudier, 1978; Bodinier *et al.*, 1986; Kaczmarek *et al.*, 2008), cutting mantle structures and pyroxenite layering.

The high-temperature deformation history of the Lanzo massif was originally attributed to the emplacement of mantle diapirs and thus the shear zone structures may have developed in response to diapiric uprise of the lherzolite body in a more or less symmetric extensional geometry (Nicolas, 1986). An alternative hypothesis was that they may have developed in an asymmetric system, as for example in the Ligurian peridotites (Vissers *et al.*, 1995).

The primary minerals of the peridotites and the gabbroic dykes were partially transformed into eclogite-facies parageneses during Alpine metamorphism (Kienast & Pognante, 1988; Pelletier & Müntener, 2006), in particular at the borders of the massif (Fig. 1). In the northwestern part the peridotite core is surrounded by serpentinized peridotites and strongly foliated serpentinites (Bente & Lensch, 1981). In places, the top of the mantle rocks is covered by ophicarbonate breccias (Pelletier & Müntener, 2006).

FIELD RELATIONS OF A HIGH-TEMPERATURE MANTLE SHEAR ZONE

Mapping and distribution of peridotite microstructures

Observations of deformation features in the field and subsequent study of thin sections allow five types of microstructure (a complete description of the microtextures is given below) to be distinguished. Deformation textures vary progressively from porphyroclastic to mylonitic. The deformation is often gradational and can change between outcrops. The five microstructural groups are: (1) porphyroclastic texture; (2) porphyroclastic fine-grained texture (PFG); (3) proto-mylonite; (4) mylonite; (5) mylonite containing ultra-mylonite bands. Modal compositions, microstructural groups and degree of alteration are summarized in Table 1. The porphyroclastic texture (1) is characterized by large, centimetre-scale, weakly deformed olivine, orthopyroxene and clinopyroxene crystals embedded in a matrix (Fig. 3a). Spinel grains are

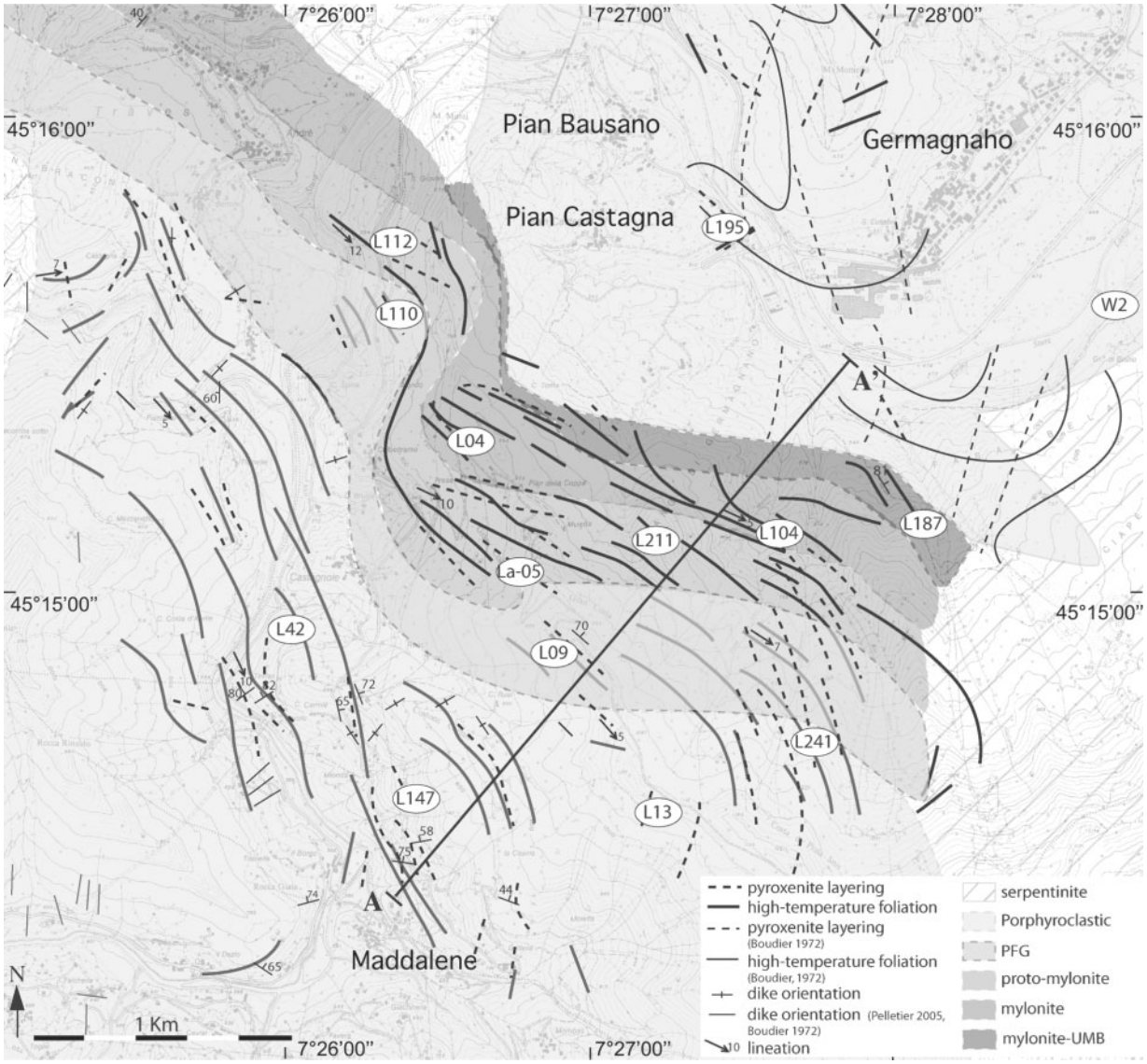

Fig. 2. Schematic map of the shear zone between the northern and the central part of the Lanzo massif. The high-temperature foliation and the pyroxenite layering are illustrated by lines. The variably deformed rocks have been separated into five groups [porphyroclastic, porphyroclastic fine-grained (PFG), proto-mylonite, mylonite and mylonite with ultra-mylonite bands (UBM)] and are illustrated by grey-scale variations from darker to lighter grey with decreasing degree of deformation. The line A–A′ corresponds to the location of the cross-section in Fig. 4. The locations of the studied samples are indicated.

usually smaller (<5 mm) and partially surrounded by a greyish white plagioclase rim. The fine-grained rocks (2) display a marked decrease in average grain size and larger proportions of entirely recrystallized domains. However, we emphasize that in the field the distinction between (1) and (2) is sometimes arbitrary. In proto-mylonitic rocks (Fig. 3b), spinel and plagioclase are aligned parallel to the foliation, whereas olivine, orthopyroxene and clinopyroxene porphyroclasts are surrounded by the foliation. The transition from porphyroclastic to mylonitic rocks is marked by a well-developed foliation and lineation. Orthopyroxene porphyroclasts can be extremely stretched, with aspect ratios exceeding 10:1 (Fig. 3c).

The foliation is reflected by elongated spinel, lenses of deformed plagioclase and elongated porphyroclasts of clinopyroxene and orthopyroxene. The pyroxenite banding is composed of variable proportions of pyroxene, plagioclase, spinel and olivine, which are recrystallized and parallel to the foliation (Fig. 3d). In the mylonite zone a passive foliation can be observed at an angle to the principal foliation (Fig. 3e, see details in 'Olivine grain size and shear sense' section below). The pyroxenite layering and the foliation are generally discordant. In the northern

Table 1: Modal composition of studied plagioclase peridotites from Lanzo

	Mylonite*	Mylonite		Proto-mylonite		PFG		Porphyroclastic central				Porphyroclastic north	
Sample:	L187d	L04	L104	L112	La-2002-5	L09	L110	L13	L42	L147	L241	W2	L195
ol	59·6	61·3	69·2	61·9	64·3	60·9	65·2	66·4	65·4	64·6	69·4	81·3	77·2
spl	0·2	0·5	1·1	0·7	0·2	0·4	0·5	0·4	1·0	0·2	0·5	0·6	0·9
plag	10·9	7·9	12·7	17·7	12·3	9·0	9·8	11·6	6·2	12·4	9·4	0·4	7·3
cpx	8·0	6·7	6·5	4·5	6·3	7·9	7·0	6·6	5·8	8·0	5·8	1·3	4·3
opx	21·2	23·5	10·6	15·2	16·9	21·8	17·5	15·0	20·2	14·8	14·9	16·4	10·4
% alteration	<10	<10	30·0	<10	<10	<10	<10	<10	<10	<10	<5	15·0	15·0

Modal composition calculated by least-squares regression of the bulk-rock compositions against mineral core or rim compositions listed in Tables 2–6. Weight % valus were converted to oxygen %, a proxy for volume %. This procedure provides a minimum for modal plagioclase. In those samples where plagioclase could not be measured because of alteration, a composition of An_{75} was assumed, similar to plagioclase listed in Table 6. Traces of hornblende are not included in mass balance. Per cent alteration includes partially serpentinized mantle minerals and altered plagioclase. PFG, porphyroclastic fine grained.
*Mylonite with ultramylonite bands.

part, the angle varies from 35 to 75°, and is about 20° in the central part (Figs 2 and 3d), both plunging steeply (50–90°) towards the NE. The thickness of the pyroxenite layers varies from 5 to 15 cm in the central part and is generally thicker in the northern part (sometimes to 40 cm). In the mylonite zone, however, the pyroxenite banding is extremely thinned (<2 cm), elongated and parallel to the foliation, which renders recognition and mapping of pyroxenite layers sometimes difficult. The lineation is mostly sub-horizontal and parallel to the foliation (Fig. 2). The Lanzo north massif, exposed on the northeastern side of the mylonite, is characterized by a clear discordance of pyroxenite banding and foliation (Figs 1 and 2). In addition, the orientation of the foliation is nearly perpendicular to that in the mylonite zone, further supporting the sharp transition from mylonite rocks to weakly deformed peridotites on the northeastern side of the shear zone.

The spatial distribution and the orientation of the different microstructures are illustrated in Fig. 2, where dashed lines separating the colours indicate the somewhat gradational transition between the microstructures. The spatial distribution of microstructures is also illustrated along a cross-section, together with lower-hemisphere stereographic projections of foliations and pyroxenite layering (Fig. 4). Along a cross-section of ~1·5 km, there is a continuous increase of deformation from porphyroclastic peridotite in the SW to the mylonite peridotite in the NE. In the SE part of the map, the high-temperature foliation and the various microstructural domains are discordant to each other, indicating that the recrystallization related to the mylonite formation overprints an older peridotite foliation. In contrast to the southwestern part, the transition from the mylonite zone to the porphyroclastic microstructure in the northern part of the Lanzo massif is relatively sharp (~200 m).

Spatial distribution of mafic dykes

Numerous gabbroic dykes and lenses are concentrated in the weakly deformed peridotites SW of the mylonite zone (Fig. 2). Most of the mafic rocks are undeformed, coarse-grained (>1 cm) olivine gabbro dykes, with little evidence of synmagmatic deformation. Dyke thickness does not exceed 40 cm in fresh peridotite, whereas larger (several tens of metres thick) gabbroic bodies were found in the serpentinized, western part of the Lanzo peridotite. Fe–Ti gabbros are rare throughout the mapped area; however, they are more abundant in the southern part of the Lanzo massif (Fig. 2). Synmagmatic deformation is localized in the centre of a few Fe–Ti gabbros. There, elevated concentrations of Ti-hornblende, ilmenite, apatite and zircon may be found, suggesting that interstitial liquids have been preferentially extracted in zones of active deformation. Details on the igneous evolution, age determinations and whole-rock geochemistry of the gabbros rocks have been presented elsewhere (Kaczmarek *et al.*, 2008).

Gabbroic dykes are sub-parallel or discordant to the foliation or layering (Figs 1 and 3f). We never observed gabbroic dykes cross-cutting the peridotite mylonite, and we are not aware of any location in Lanzo North where gabbroic dykes have been found. However, we found hornblende-bearing gabbroic dykes in the mylonite zone. They were probably emplaced as sills or, alternatively, parallelized and deformed after their emplacement. They display millimetre-scale reaction rims to the host peridotite. This suggests that the mechanical contrast between

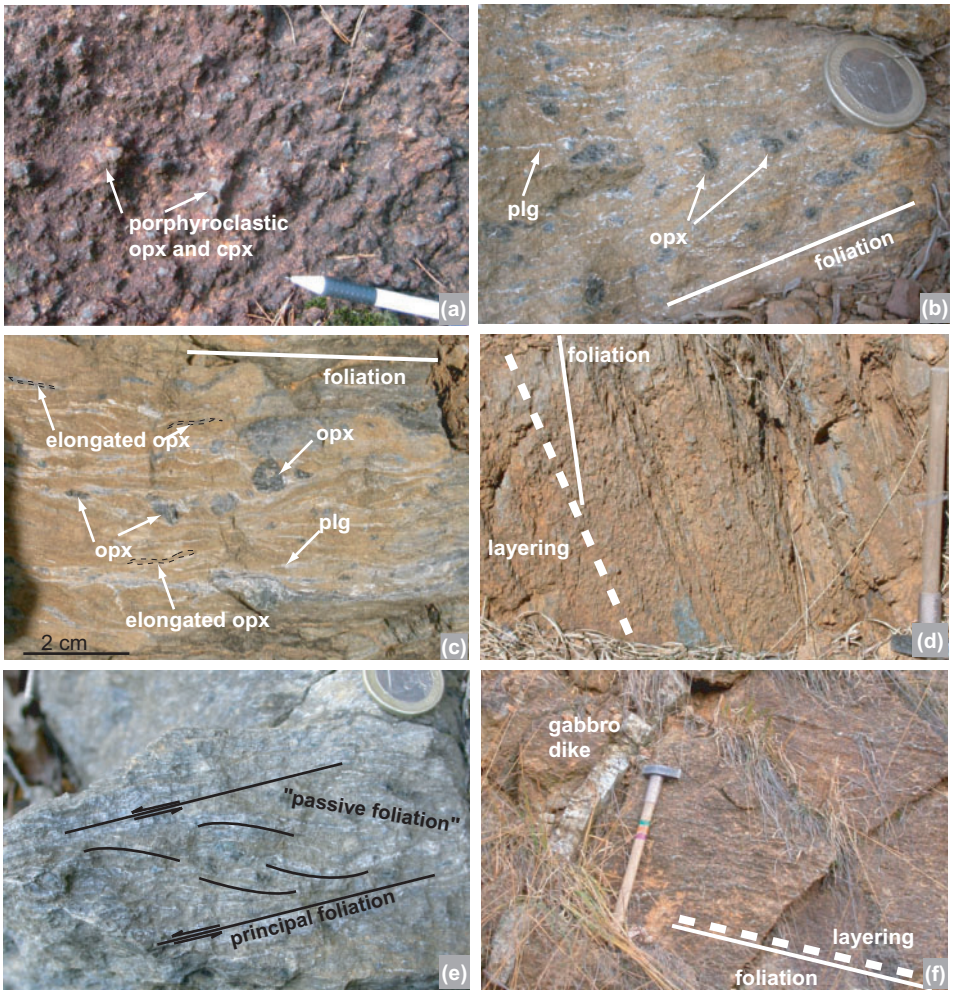

Fig. 3. Photographs of representative outcrops in the central part of the Lanzo massif. (a) Porphyroclastic texture with centimetre-scale pyroxenes weathering out from the surface (south of Pian Castagna). (b) Proto-mylonitic peridotite with pyroxene porphyroclasts and high-temperature foliation highlighted by white bands of plagioclase (east of Colbeltramo). (c) High-temperature foliation and porphyroclasts in the mylonite rock; it should be noted that some of the orthopyroxene grains are elongated, whereas others form rounded porphyroclasts (east of Colbeltramo). (d) Angular discordance between spinel pyroxenite layering and high-temperature foliation (Gran Costa). (e) Example of an internal oblique foliation indicating a sinistral shear sense in the mylonite zone (east of Colbeltramo). (f) Gabbro dyke cross-cutting deformed peridotite (northeastern of Maddalene). opx, orthopyroxene; cpx, clinopyroxene; plg, plagioclase.

the mylonite and the weakly deformed peridotite was high enough to prevent propagation of gabbroic dykes across the mylonite zone. The consequences of these observations will be discussed below.

PERIDOTITE MICROSTRUCTURES

As outlined above, the peridotite microstructures can be divided into five groups based on field observations and microstructural investigations of ~100 thin sections (cut perpendicular to the foliation and parallel to the lineation). The classification of the microstructures is based on Spry (1969), Mercier & Nicolas (1975) and Sibson (1977). Textures related to melt–rock interaction are described separately.

Microstructures related to deformation

Porphyroclastic texture (Fig. 5a)

The porphyroclastic texture is characterized by a bimodal grain-size distribution, containing weakly deformed porphyroclasts (olivine, orthopyroxene, clinopyroxene) with grain sizes exceeding 1 cm, embedded in matrix of recrystallized grains made of olivine, orthopyroxene, plagioclase, clinopyroxene and spinel. The development of textures with 120° triple junctions can be observed in areas formed by orthopyroxene, clinopyroxene, olivine and plagioclase (Fig. 5a), and in olivine-rich areas, which suggests partial

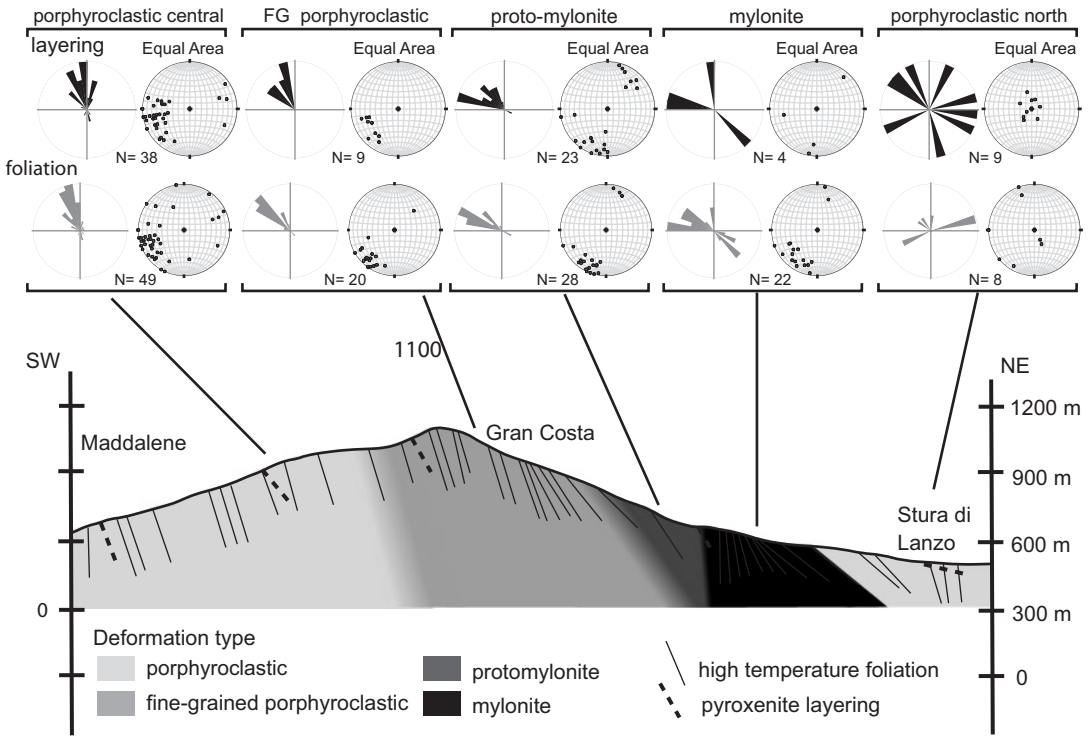

Fig. 4. Cross-section of the shear zone illustrating layering and foliation relationships associated with the style of deformation. Foliation and layering are represented by lower hemisphere, equal area projections. Rose diagrams represent plane orientation and the associated stereographs correspond to the pole of the foliation or pyroxenite layering (•). It should be noted that the foliation and the layering of the Lanzo North peridotite are discordant to the mylonite zone.

re-equilibration induced by reheating or melt interaction. Exsolved mantle orthopyroxene porphyroclasts are sometimes kinked and show curvilinear grain boundaries where they are partially replaced by new olivine, indicating replacement of mantle orthopyroxene by olivine. Occasionally, subhedral olivine crystals are included in large orthopyroxene. Olivine is characterized by deformation lamellae and embayment structures, where newly crystallized olivine can be found. Porphyroclastic clinopyroxene with orthopyroxene exsolution lamellae is mostly recrystallized to smaller grains of ~0·5 mm. Recrystallized brown spinel (>1 mm) is rounded or aligned parallel to the foliation, and in places associated with plagioclase aggregates. Smaller dark brown spinels (<0·4 mm) are associated with new orthopyroxene and/or follow olivine grain boundaries. Plagioclase (around millimetre grain size) is associated with spinel and distributed randomly in the sample. In most samples, vermicular, pargasitic Ti-hornblende (10–50 μm, Fig. 5b) rims clinopyroxene porphyroclasts or builds elongated interstitial grains suggesting grain boundary migration and crystallization of interstitial liquids or fluids.

Porphyroclastic fine-grained texture (PFG; Fig. 5c)

This texture is characterized by an increase in the modal proportions of recrystallized grains compared with relict porphyroclasts (Fig. 5b). Similar to the porphyroclastic texture, the development of triple junctions can be observed. Porphyroclasts of exsolved orthopyroxene and clinopyroxene are less than 1 cm in size. Olivine porphyroclasts display an increase in subgrain bands and larger areas of dynamically recrystallized grains. Recrystallized olivine, orthopyroxene, clinopyroxene, spinel and plagioclase display a shape-preferred orientation subparallel to the foliation. Spinel shows different grain shapes that correlate with its microstructural site. Rounded spinels (≤0·3 mm) can be included in olivine or orthopyroxene, whereas vermicular spinel is found along olivine grain boundaries. Elongate (long axis ~1 mm), dark brown spinel aligned with the foliation is usually associated with plagioclase. Twin lamellae of plagioclase (grain size ~0·2 mm) can be preferentially oriented parallel to the spinel foliation; however, unoriented, spinel-free plagioclase lenses have also been observed. As above, interstitial Ti-hornblende preferentially surrounding clinopyroxene has been observed.

Proto-mylonite texture (Fig. 5d)

This texture is characterized by further grain-size reduction of porphyroclasts and the first occurrence of elongate orthopyroxene, with gliding along (001) slip planes. Aspect ratios may approach 10:1. The plagioclase distribution in

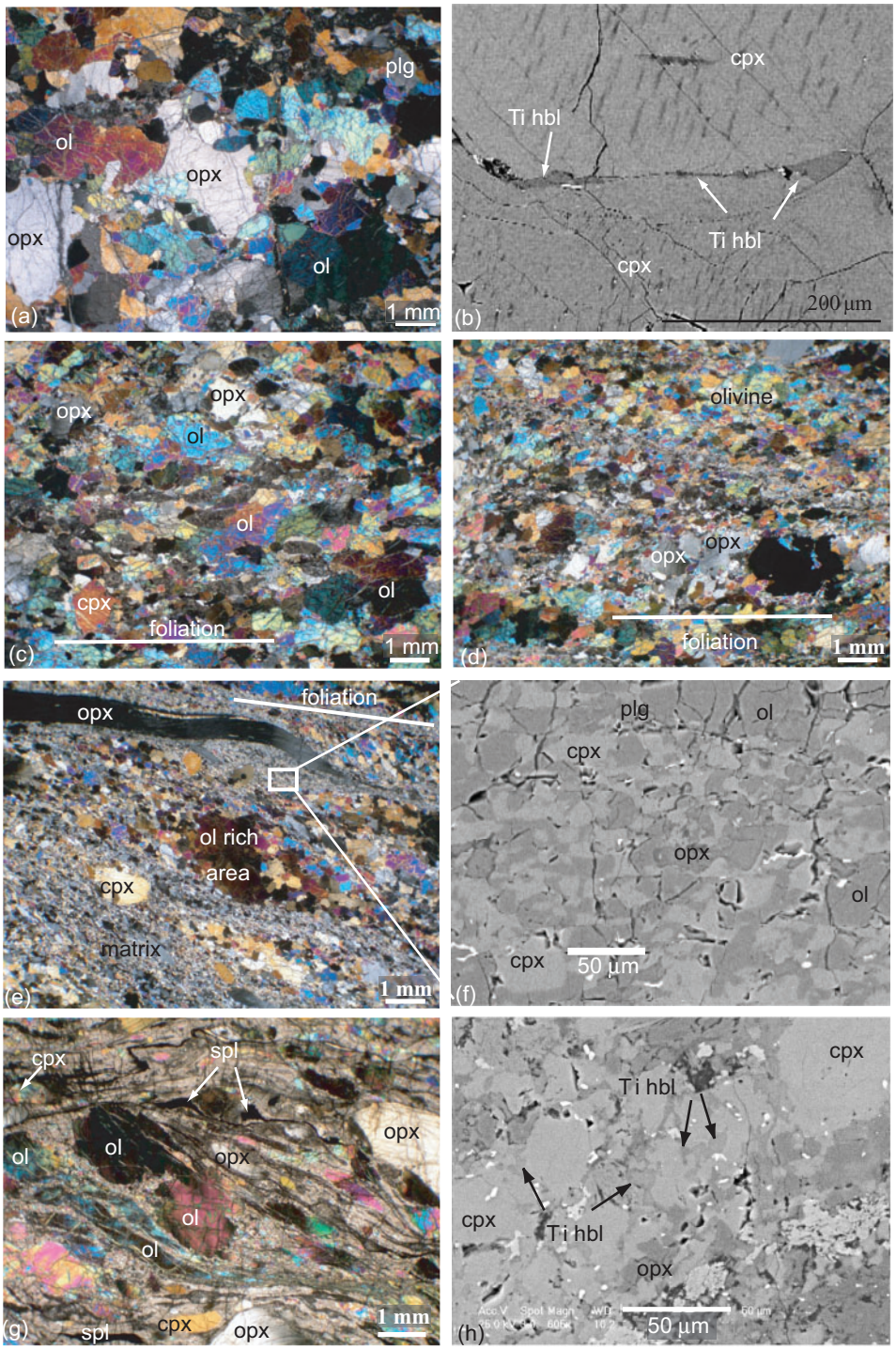

Fig. 5. Photomicrographs and backscattered electron (BSE) images of rock types. (a) Porphyroclastic texture (Ll47, crossed nicols). (b) BSE image of Ti-hornblende (Ti-hbl) at the border of porphyroclastic clinopyroxene (Ll3). It should be noted that the exsolution lamellae disappear in the last 20–30 µm, indicating recrystallization of clinopyroxene along its borders. (c) Porphyroclastic fine-grained texture (Ll10, crossed nicols). (d) Proto-mylonite texture (Ll12, crossed nicols). (e) Mylonite texture (L04), characterized by elongated orthopyroxene with aspect ratios exceeding 20:1, and recrystallized olivine oriented oblique to the main foliation (crossed nicols). (f) BSE image of the fine-grained matrix in the mylonite (L04). (g) Mylonite with ultra-mylonite bands localized in the north part of the shear zone (Ll87d). The flow fabrics in the fine-grained polyphase matrix surrounding deformed olivine, orthopyroxene and spinel clasts should be noted (crossed nicols). (h) BSE image of Ti-hbl rich zone associated with clinopyroxene, orthopyroxene and spinel neoblasts in mylonite with ultra-mylonite bands (Ll87d). opx, orthopyroxene; cpx, clinopyroxene; ol, olivine; plg, plagioclase; spl, spinel; Ti-hbl, Ti-rich hornblende.

these samples is similar to that described above: either associated with spinel or scattered in the sample with a grain size around 0·5–1 mm. There is a small angle between the foliation and the shape-preferred orientation of olivine (Fig. 5d). The proportion of recrystallized matrix minerals (olivine, clinopyroxene, orthopyroxene, plagioclase, spinel, and Ti-hornblende) generally exceeds 25–30%. The grain size of the matrix minerals varies between 50 and 200 μm. Spinel (grain size exceeding 1 mm) is aligned with the foliation and can be associated with plagioclase lenses or olivine.

Mylonite texture (Fig. 5e)

The mylonitic texture can be distinguished from the proto-mylonite by the occurrence of porphyroclasts embedded in a fine-grained matrix, and by the presence of extremely stretched orthopyroxene with aspect ratios exceeding 20:1. In several places, the fine-grained bands are well developed parallel to stretched orthopyroxenes, whereas in other areas there is a distinct angle between fine-grained bands and elongate minerals. Olivine-rich areas are elongate, oblique to the foliation and composed of porphyroclastic relics with subgrain domains, surrounded by a matrix of dynamically recrystallized olivine (50–100 μm). Secondary phases are rare and restricted to small brown or black vermicular spinel pinning olivine grain boundaries. Plagioclase is scattered in the sample, but can form aggregates of several grains in the fine-grained matrix. In the latter case they are about one order of magnitude larger than other mixed phases. Plagioclase displays corrugated extinction and deformation twins indicating post-crystallization deformation. Occasionally, plagioclase surrounds porphyroclastic spinel (<2 mm) and forms lenses in the foliation.

The fine-grained matrix displays an inhomogeneous distribution within the mylonite and is made of olivine, clinopyroxene, orthopyroxene, plagioclase, spinel, and some Ti hornblende (Fig. 5f). The recrystallized grain size varies from 5 to 50 μm, about one order of magnitude smaller than in the olivine-rich areas. Minerals in the matrix have a weak shape preferred orientation, which defines the main foliation. Spinel grains are small (~10 μm), with black or brownish colours. Some plagioclase grains in the matrix are larger than the other minerals (>50 μm) and seemingly less deformed than matrix minerals.

The mylonitic microstructure shows three distinctive zones with variable grain size: (1) porphyroclastic zones; (2) intermediate zones composed of smaller grains of 100–200 μm; (3) a very fine-grained matrix (5–50 μm). Observations reveal that there is a sharp transition between the fine-grained matrix and the other two domains, indicating that strain strongly partitions into the fine-grained matrix.

Mylonite with ultra-mylonite bands texture (Fig. 5g)

The mylonite with ultra-mylonite bands is located in the northern part of the mylonite area, at the limit of the northern body (Fig. 2), and is characterized by elongated olivine, elongated or rounded orthopyroxene and clinopyroxene embedded in an ultra-mylonite matrix. In this texture, the extremely fine-grained bands are penetrative and cross-cut porphyroclasts. Olivine porphyroclasts are elongated, and exhibit deformation and kink bands suggesting deformation at lower temperature. In some cases these porphyroclasts are relatively coarse-grained aggregates of recrystallized olivine (10–50 μm). Exsolved orthopyroxene and clinopyroxene porphyroclasts are stretched and sometimes broken into several pieces, suggesting that gliding along (001) was no longer active. Porphyroclastic spinel size is between 200 and 400 μm. In most cases spinel grains are flattened and aligned parallel to the foliation. Bands of disrupted spinel grains are formed in the pressure shadows of larger porphyroclasts (Fig. 5g). These microstructures indicate that the large porphyroclastic grains behaved as 'rigid' particles during deformation.

The fine-grained ultra-mylonitic matrix is composed of orthopyroxene, clinopyroxene, spinel, plagioclase (completely altered), olivine and Ti-hornblende with grain size between <5 and 15 μm. Ti-hornblende is more abundant in the penetrative ultra-mylonite bands than in mylonite and partially replaces clinopyroxene neoblasts (Fig. 5h), suggesting the presence of interstitial melt and/or fluids during deformation. Plagioclase is rare and might preferentially be destabilized by fluid percolation. The matrix locally contains retrograde hydrous minerals (chlorite, serpentine and amphibole), which replace anhydrous minerals.

Olivine grain size and shear sense

Olivine grain size was determined with digitized optical images analysed with the SXimage software (Barrett S. 2005; Version 1.75) for each deformation type. The analysis was performed on recrystallized olivine-rich areas, which partially replace olivine porphyroclasts. In the case of proto-mylonite and mylonite samples, recrystallized grains are smaller and show an oblique grain-shape preferred orientation (Fig. 6). Such an oblique grain-shape fabric, however, has generally not been observed in porphyroclastic samples. Results of aspect ratio and absolute length determinations of olivine long axes for the two deformation types (mylonite and porphyroclastic) are illustrated in histograms in Fig. 6. The two categories show maximum aspect ratios close to 1·5, but may reach values up to 5·0 in mylonitic samples. However, the length of the morphological olivine long axis is clearly different: the histogram indicates that most of the grains in mylonites are smaller than 0·2 mm, with only a few grains

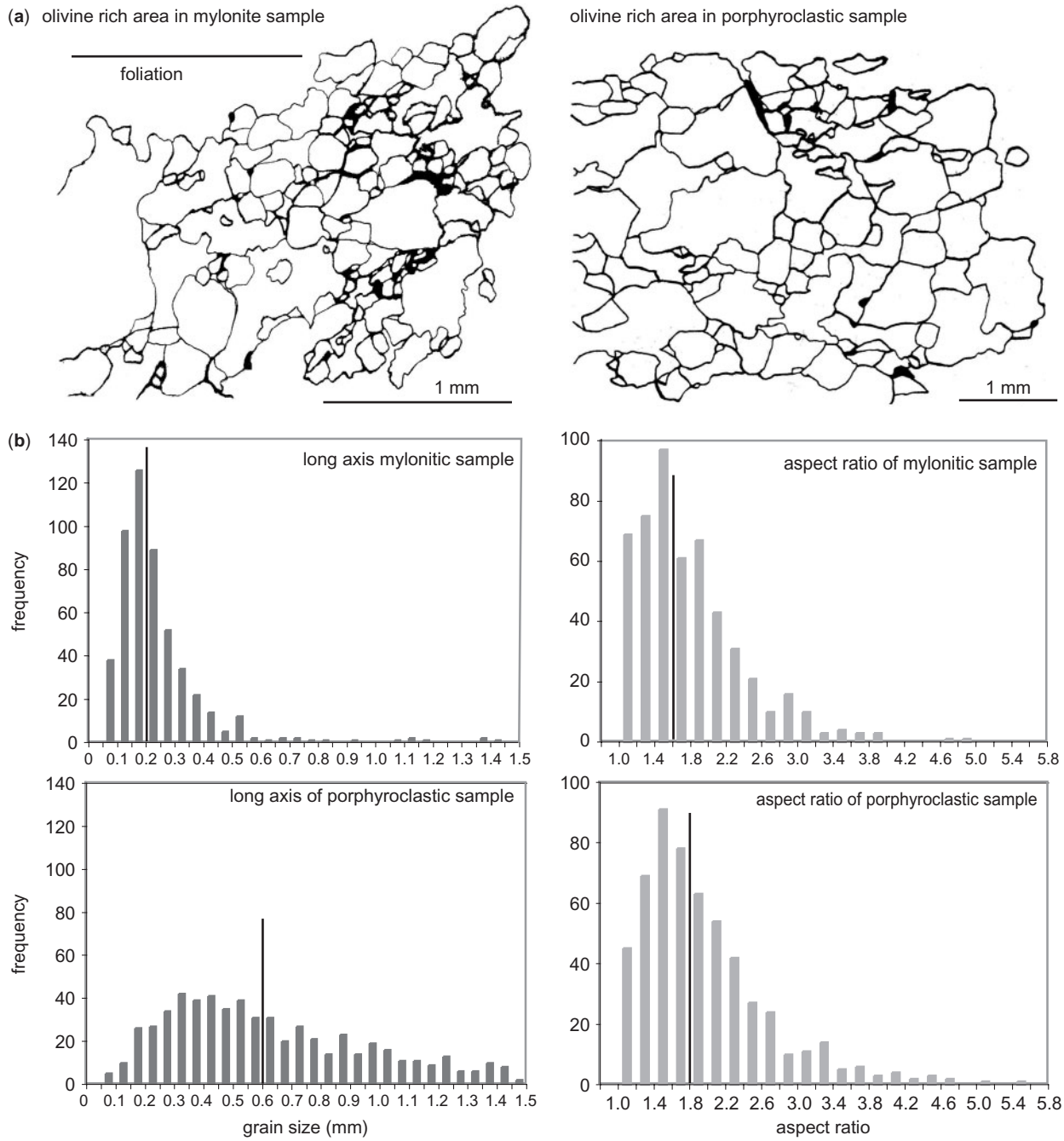

Fig. 6. (a) Drawings from photomicrographs delineating recrystallized olivine grain size and shape in mylonite and porphyroclastic samples. The elongated grain orientation in the mylonite is oblique to the foliation, whereas in porphyroclastic rocks the elongation of the grains is roughly parallel to the foliation. (b) Results of grain-size analysis [long axis (in mm) and aspect ratio] in mylonite ($n = 6$) and porphyroclastic sample ($n = 9$) obtained on ~600 grains (>100 per sample). It should be noted that the mylonite shows a much tighter grain-size distribution, with close correspondence of median and maximum, whereas the porphyroclastic sample has a median value that is substantially higher; also, the aspect ratio is not dramatically different between the two samples.

exceeding 0·4 mm. In contrast, in the porphyroclastic samples there is a large variability in olivine long axis length with a median at 0·6 mm; however, maximum grain sizes reach 18 mm.

Peridotite shear sense indicators were either obtained from field observations such as the lens-shaped appearance of peridotite mylonite (Fig. 3c), or from oriented thin sections. Shape preferred orientation of olivine-rich areas,

stretched orthopyroxene porphyroclasts and dynamically recrystallized matrix minerals oblique to the foliation at an angle of 25–30° were used to derive the microscopic shear sense. Shear sense determinations indicate a preferential sinistral sense of shear. These microscopic and macroscopic shear sense determinations are consistent with the large-scale structures on a map scale (Fig. 2), which tend to be parallel to the mylonite in the northern and southern part and indicate an overall sinistral sense of shear.

Microstructures related to melt impregnation

Microstructures related to reactive fractionation of silicate liquids are found all over the Lanzo massif, particularly in the southern part (Müntener & Piccardo, 2003), indicating that melt migration is a regional-scale phenomenon. Here we restrict our analysis to observations relevant for the deformation history of the Lanzo mantle shear zone. Evidence for melt–rock reaction can be observed in all peridotite types. The melt–rock reaction is expressed by vermicular and interstitial, mostly exsolution-free and undeformed orthopyroxene, localized along the contact with olivine and/or cross-cutting larger porphyroclastic olivine. These microstructures probably indicate the reaction of SiO_2-saturated melts with olivine according to the peritectic reaction (Fig. 7b, c and h)

$$\text{Liq. } 1 + \text{olivine} \rightarrow \text{orthopyroxene} + \text{Liq. } 2. \quad (1)$$

Plagioclase has been observed in three microstructural sites: (1) plagioclase surrounding dark Cr-rich spinel is oriented sub-parallel to the foliation in the mylonitic rocks (Fig. 7d); (2) plagioclase forms aggregates parallel to the foliation associated with orthopyroxene, clinopyroxene and olivine; (3) some exsolved porphyroclastic clinopyroxenes are partially replaced by orthopyroxene patches and/or by intergrowths of orthopyroxene and plagioclase (Fig. 7e–g), similar to observations from Lanzo south, where orthopyroxene and plagioclase show cotectic intergrowth (Müntener & Piccardo, 2003). This microstructure is preferentially preserved in weakly deformed rocks, or within large porphyroclasts in proto-mylonite or mylonite. The migrating melt followed or cross-cut pre-existing exsolution lamellae in the deformed and undeformed clinopyroxenes, indicating melt–rock reaction before or during the shearing. This suggests that clinopyroxene became unstable in the presence of a clinopyroxene-undersaturated melt:

$$\text{cpx} + \text{Liq} \rightarrow \text{opx} + \text{plg} \pm \text{ol}. \quad (2)$$

MINERAL CHEMISTRY

Mineral compositions were determined using a Cameca SX-50, a Jeol JXA 8200 electron microprobe located at the Institute of Geological Sciences at the University of Bern (Switzerland), and a Cameca SX5l at the Institute of Mineralogy at the University of Heidelberg (Germany), equipped with four or five wavelength-dispersive spectrometers, respectively. No systematic differences between the electron microprobes have been observed. Operating conditions comprised an acceleration voltage of 15 kV and a 20 nA beam current. The spot size was about 3 μm for all minerals except plagioclase and amphibole, for which a less focused beam was used (~5 μm). Element peak and background counting time was 20 s, except for Al (30 s), Mg (30 s) and Na (10 s). Natural and synthetic oxides were used as standards. Backscattered electron (BSE) images were obtained at the CSEM (Centre Suisse d'Electronique et de Microtechnique) at Neuchâtel (Switzerland), with an Environmental Scanning Electron Microscope, Philips XL-30, operated at 25 kV. Averages of mineral compositions from various microstructural sites and their standard deviations are listed in Tables 2–7. The complete dataset is available as Supplementary Data at http:petrology.oxfordjournals/org.

Clinopyroxene

Clinopyroxene from the Lanzo massif shows large compositional variations (Table 2), which are dependent on the microstructural site but are apparently independent of the regional structure. In all samples, the compositional variation is nearly as large as the entire dataset. Exsolution of orthopyroxene lamellae is common in clinopyroxene porphyroclasts, but less common in recrystallized grains. In addition to these representative textures, occasional clinopyroxene clasts show flame-like orthopyroxene and plagioclase inclusions, in proportions much higher than can be exsolved from primary clinopyroxene (see Fig. 7f). These grains show extreme disequilibrium compositions.

Overall, the clinopyroxene data reflect two compositional trends with decreasing Al_2O_3 content (Fig. 8), which correspond to retrogression from spinel to plagioclase facies. The first trend is recorded by porphyroclastic cores and is characterized by a negative correlation between Al and Ti or Cr. This negative correlation (enrichment in Cr and Ti) may reflect interaction with basaltic melt. The second trend, seen in the neoblasts, is characterized by a positive correlation between Al, Cr and Ti, and represents cooling. In terms of absolute element concentrations, the Al_2O_3 content in clinopyroxene porphyroclast cores ranges from 4·3 to 7·5 wt % and is substantially higher than in neoblasts (1·37–4·85 wt %). Mg-number is not correlated with Al_2O_3 and varies from ~0·9 to 0·94. CaO contents are generally high, as observed for orogenic and residual abyssal peridotites (Hellebrand *et al.*, 2005), indicating substantial retrograde equilibration (see 'Thermometry' section below).

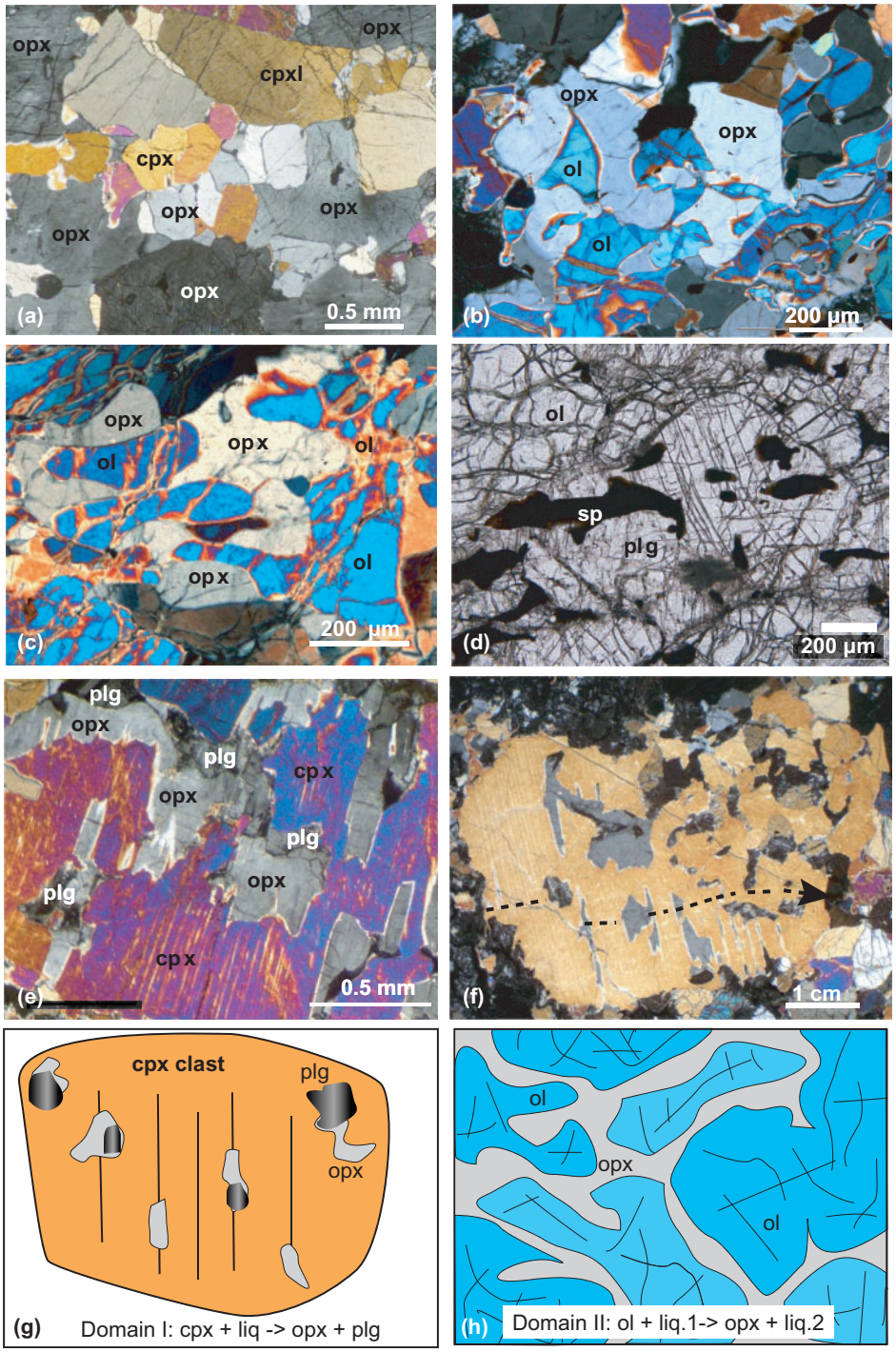

Fig. 7. Photomicrographs of textures related to recrystallization, melt impregnation and melt–rock reaction. (a) Recrystallized zone of clinopyroxene and orthopyroxene between larger pyroxene porphyroclasts (Ll3, crossed nicols). (b) Fine-grained olivine + orthopyroxene domain in pressure shadows of large olivine porphyroclast. The interstitial, anhedral form of orthopyroxene should be noted (I2, crossed nicols). (c) Orthopyroxene replacing deformed olivine, suggesting replacement after high-temperature deformation. (d) Undeformed plagioclase replacing deformed and elongated spinel, indicating crystallization of plagioclase after deformation of spinel (L24l, plane-polarized light). (e) Peritectic replacement of clinopyroxene porphyroclasts by orthopyroxene and plagioclase (Ll3); the irregular crystal shapes of opx and plg should be noted (crossed nicols). (f) Clinopyroxene porphyroclast, partially replaced by orthopyroxene and plagioclase. Arrow indicates microprobe traverse A–A′ shown in Fig. 9 (crossed nicols). (g) Schematic representation of clinopyroxene partially replaced by orthopyroxene and plagioclase in the presence of melt (domain I). (h) Schematic illustration of interstitial orthopyroxene replacing olivine, according to the reaction ol + liq1 → opx + liq2 (domain II). Abbreviations as in Fig. 5.

Table 2: Clinopyroxene compositions of neoblasts, and porphyroclast cores and rims

	Mylonite UMB			Mylonite						Proto-mylonite					
Sample:	L187d			L04			L104			L112			La-2002-5		
	neoblasts	rim	core	neoblast	Rim	Core	neoblast	rim	core	neoblast	rim	core	neoblasts	rim	core
	n = 4	*n* = 2	*n* = 4	*n* = 4	*n* = 2	*n* = 3	*n* = 4	*n* = 2	*n* = 3	*n* = 2	*n* = 2	*n* = 3	*n* = 4	*n* = 3	*n* = 4
wt %															
SiO_2	53·7(3)	52·0(4)	50·1(2)	53·2(3)	52·4(2)	50·1(3)	52·2(5)	51·6(1)	50·1(2)	52·9(0)	52·3(0)	50·4(2)	53·5(9)	52·3(4)	51·3(1)
TiO_2	0·54(6)	0·85(7)	0·82(3)	0·66(4)	0·64(6)	0·60(3)	0·76(4)	0·79(0)	0·77(6)	0·66(2)	0·79(1)	0·84(3)	0·57(19)	0·68(4)	0·76(3)
Al_2O_3	1·8(1)	3·6(4)	6·5(1)	2·62(14)	3·38(7)	7·0(1)	3·7(4)	4·09(4)	6·6(1)	2·36(8)	3·3(3)	5·75(6)	2·2(7)	3·6(3)	4·6(1)
Cr_2O_3	0·39(5)	1·1(0)	0·92(3)	0·63(10)	0·93(2)	1·04(3)	0·91(6)	1·04(4)	1·1(0)	0·56(0)	0·83(6)	1·26(2)	0·56(19)	1·01(8)	1·2(1)
Fe_2O_3	1·0(4)	1·2(4)	1·8(4)	1·2(5)	1·92(4)	1·99(68)	1·8(5)	2·3(4)	2·1(5)	1·5(8)	1·0(0)	2·07(9)	0·69(58)	0·65(5)	1·3(3)
FeO	1·6(3)	1·5(2)	1·6(4)	1·5(4)	1·05(2)	1·37(50)	1·5(4)	0·71(23)	1·6(3)	1·4(9)	2·0(0)	1·37(24)	2·1(4)	2·24(4)	1·8(3)
MnO	0·08(3)	0·10(1)	0·14(4)	0·06(3)	0·11(3)	0·10(3)	0·08(3)	0·10(2)	0·08(2)	0·08(4)	0·10(3)	0·10(5)	0·09(2)	0·04(3)	0·08(2)
NiO	0·06(2)	0·04(3)	0·07(2)	0·02(2)	0·03(2)	0·04(2)	0·04(2)	—	—	0·06(1)	0·05(2)	0·02(1)	0·05(2)	0·05(3)	0·04(2)
MgO	17·1(1)	16·1(2)	14·8(2)	17·2(1)	17·1(1)	15·1(2)	16·7(2)	16·3(0)	15·6(5)	16·9(1)	16·4(1)	15·1(2)	17·0(5)	16·3(2)	15·7(1)
CaO	24·0(1)	23·3(1)	22·8(1)	23·1(1)	22·5(4)	22·5(3)	22·4(3)	23·0(4)	21·7(5)	23·5(4)	23·0(2)	22·8(3)	23·2(3)	22·7(2)	22·7(1)
Na_2O	0·40(3)	0·62(6)	0·73(3)	0·52(3)	0·57(2)	0·69(2)	0·64(4)	0·67(11)	0·71(2)	0·45(7)	0·55(2)	0·70(2)	0·44(8)	0·56(1)	0·65(1)
K_2O	<0·01	<0·01	<0·01	<0·01	0·01(1)	0·01(1)	<0·01	<0·01	<0·01	0·01(1)	<0·01	0·01(1)	0·01(1)	<0·01	0·01(1)
Total	100·5(2)	100·3(0)	100·2(5)	100·7(1)	100·6(28)	100·4(1)	100·7(4)	100·6(1)	100·3(2)	100·2(5)	100·2(3)	100·4(3)	100·3(3)	100·1(4)	100·2(2)
Mg-no.	0·928	0·920	0·897	0·925	0·922	0·900	0·948	0·970	0·940	0·920	0·913	0·898	0·920	0·913	0·906
Cr-no.	0·128	0·165	0·086	0·138	0·155	0·091	0·140	0·146	0·100	0·137	0·145	0·128	0·149	0·159	0·154

	PFG						Porphyroclastic central							
Sample:	L09			L110			L13			L42		L147		
	neoblasts	rim	core	neoblasts	Rim	core	neoblasts	rim	core	rim	core	neoblast	rim	core
	n = 3	*n* = 2	*n* = 4	*n* = 3	*n* = 3	*n* = 4	*n* = 4	*n* = 2	*n* = 4	*n* = 3	*n* = 5	*n* = 3	*n* = 3	*n* = 4
wt %														
SiO_2	52·1(1)	52·0(3)	49·7(3)	53·0(8)	51·8(1)	50·0(1)	50·9(1)	52·4(1)	50·1(3)	51·0(1)	49·6(3)	50·9(2)	52·0(2)	50·7(2)
TiO_2	0·67(1)	0·73(1)	0·84(5)	0·60(20)	0·91(4)	0·80(9)	1·01(3)	0·98(1)	0·55(3)	0·64(4)	0·49(6)	0·78(4)	0·91(4)	0·81(2)
Al_2O_3	3·8(2)	3·21(1)	6·63(7)	2·5(8)	3·7(1)	6·5(1)	4·9(1)	3·4(4)	7·35(3)	4·1(1)	6·0(1)	4·7(2)	4·0(4)	5·8(1)
Cr_2O_3	1·0(2)	1·1(2)	1·27(4)	0·64(15)	1·1(1)	0·98(3)	1·4(1)	0·99(10)	1·22(5)	1·2(1)	1·4(1)	1·2(1)	1·1(1)	1·2(0)
Fe_2O_3	1·7(1)	1·57(6)	1·8(4)	0·89(50)	0·65(29)	1·2(1·4)	1·7(2)	1·01(33)	1·4(5)	1·9(1·0)	2·7(5)	0·13(23)	0·81(42)	1·5(4)
FeO	1·8(2)	1·27(4)	1·5(3)	2·0(2)	1·8(2)	1·7(1·2)	1·7(2)	2·2(4)	2·2(4)	0·92(85)	0·46(47)	2·9(2)	1·9(4)	1·8(3)
MnO	0·09(4)	0·10(4)	0·07(2)	0·07(3)	0·07(6)	0·09(5)	0·10(4)	0·14(5)	0·08(3)	0·12(1)	0·11(2)	0·06(3)	0·06(3)	0·08(4)
NiO	0·03(2)	—	0·00(1)	0·06(4)	0·01(2)	0·04(1)	0·07(3)	0·05(0)	0·07(3)	0·05(4)	0·05(1)	0·03(4)	0·05(2)	0·06(2)
MgO	16·9(2)	16·58(5)	15·0(2)	16·8(4)	15·8(1)	15·6(1·8)	15·742)	16·5(2)	14·3(2)	16·0(6)	15·3(2)	15·3(1)	15·9(2)	15·2(1)
CaO	22·3(4)	22·85(2)	22·5(3)	23·2(3)	23·4(1)	22·0(1·2)	22·4(2)	22·7(6)	22·7(3)	22·6(6)	22·5(5)	23·0(2)	23·6(4)	23·0(1)
Na_2O	0·53(4)	0·58(4)	0·67(5)	0·46(5)	0·58(1)	0·61(11)	0·68(7)	0·56(1)	0·72(5)	0·65(4)	0·67(2)	0·57(2)	0·51(9)	0·64(5)
K_2O	<0·01	<0·01	<0·01	0·01(1)	0·01(1)	0·01(1)	0·01(1)	0·01(1)	0·01(1)	<0·01	0·01(1)	<0·01	0·01(1)	0·00(1)
Total	100·5(1)	100·0(6)	99·9(5)	100·2(2)	99·8(3)	99·5(6)	100·5(2)	101·0(0)	100·8(3)	99·2(6)	99·3(3)	99·5(2)	100·9(3)	100·7(2)
Mg-no.	0·913	0·921	0·903	0·916	0·924	0·912	0·900	0·907	0·882	0·920	0·911	0·902	0·916	0·902
Cr-no.	0·154	0·185	0·114	0·148	0·165	0·092	0·157	0·162	0·100	0·168	0·133	0·151	0·153	0·123

(continued)

Table 2: Continued

Sample:	Porphyroclastic central			Porphyroclastic north				
	L241			W2			L195	
	neoblast	rim	core	neoblasts	rim	core	rim	core
	$n=3$	$n=2$	$n=4$	$n=3$	$n=3$	$n=2$	$n=1$	$n=6$
wt %								
SiO_2	52·2(9)	51·4(4)	50·4(1)	52·0(7)	51·7(4)	50·5(1)	52·6	50·4(2)
TiO_2	0·72(13)	0·78(6)	0·68(3)	0·55(1)	0·68(9)	0·60(4)	0·45	0·38(6)
Al_2O_3	3·2(1·0)	4·0(1)	6·0(1)	3·4(1)	3·7(3)	5·4(2)	3·8	7·2(1)
Cr_2O_3	0·77(21)	0·97(8)	1·15(5)	0·96(4)	1·19(5)	1·4(1)	1·1	1·2(1)
Fe_2O_3	1·5(5)	1·7(3)	2·1(5)	1·8(1·1)	1·8(7)	2·3(6)	<0·01	0·17(22)
FeO	1·6(3)	1·5(2)	1·4(4)	1·1(8)	0·95(78)	0·83(57)	2·5	2·6(3)
MnO	0·10(2)	0·08(1)	0·11(3)	0·09(1)	0·11(2)	0·11(3)	0·09	0·10(3)
NiO	0·03(3)	0·02(0)	0·03(3)	0·04(2)	0·03(3)	0·05(0)	0·06	0·04(1)
MgO	16·5(4)	16·0(1)	15·1(1)	16·3(1)	15·8(2)	15·0(2)	16·0	14·6(2)
CaO	23·1(3)	23·1(5)	22·8(2)	23·3(1)	23·8(5)	23·2(3)	22·3	22·4(5)
Na_2O	0·51(8)	0·54(4)	0·70(3)	0·59(1)	0·61(5)	0·72(2)	0·52	0·65(6)
K_2O	<0·01	<0·01	0·01(2)	0·01(1)	<0·01	<0·01	0·01	0·01(0)
Total	100·1(3)	100·0(5)	100·3(3)	100·0(3)	100·3(3)	100·1(5)	99·4	99·7(2)
Mg-no.	0·914	0·909	0·899	0·918	0·921	0·909	0·920	0·906
Cr-no.	0·139	0·142	0·116	0·842	0·824	0·854	0·158	0·100

Mg-number $= Mg/(Mg + Fe_{tot})$; Cr-number $= Cr/(Cr + Al)$. UMB, ultra-mylonite bands; PFG, porphyroclastic fine-grained.

Chemical compositions in some porphyroclastic clinopyroxenes (Sample L13, Table 2) are heterogeneous and strongly zoned. This is illustrated in Fig. 9, where a clinopyroxene core with a plateau of high Al (0·31 Al p.f.u.) and low Ti (0·015 p.f.u.) is preserved, with a composition similar to clinopyroxene from fertile spinel peridotites (Ernst & Piccardo, 1979; Müntener *et al.*, 2004). Through areas with orthopyroxene–plagioclase intergrowths (Fig. 7), Al decreases whereas Ti and Cr increase (Fig. 9).

Orthopyroxene

All analysed grains are enstatite-rich with Mg-number ranging from 89·0 to 91·2 with no notable difference between cores and rims. Substantially lower Mg-numbers were measured only for pyroxenite layers. Clinopyroxene exsolution lamellae in orthopyroxene are generally very thin (<1 μm) and too small to be analysed by electron microprobe. Orthopyroxene was analysed with a focused beam size of ~3 μm, and exsolution lamellae were not included in the chemical composition of the orthopyroxene. In addition, many samples exhibit signs of extensive dynamic recrystallization and therefore clinopyroxene exsolution lamellae were not detected. CaO and Al_2O_3 contents are variable, related to mineral zoning and different microstructural sites (Figs 10 and 11a). Orthopyroxene neoblasts show lower values of Al_2O_3 (0·64–2·95 wt %), and Cr_2O_3 (0·12–0·65 wt %) than in porphyroclast cores (2–5 wt % and 0·55–1 wt %, respectively; Fig. 11a). The samples from the northern part of the massif (W2 and L195) exhibit high Al_2O_3 values for the core composition (up to 4·80 wt %).

Large porphyroclastic orthopyroxene grains (~2500 μm) display pronounced zoning from core to rim. In several orthopyroxene porphyroclasts, Al decreases from the core (0·15–0·20 p.f.u.) to the rim (0·04–0·09 p.f.u.). However, the Ca content is uniformly low and shows virtually no zoning (Fig. 10). In some porphyroclasts, a plateau of intermediate composition between the core and the rim can be recognized (e.g. L147, L241).

In most samples, some of the orthopyroxene appears to have formed by melt–rock reaction, either displaying cotectic crystallization textures together with plagioclase, replacing clinopyroxene (domain I) or forming at the expense of olivine (domain II, Fig. 7). In these samples the composition of orthopyroxene seems to be locally controlled: (1) high Al in orthopyroxene (relative to the addition of melt), but low Ca (which is buffered by

Table 3: Orthopyroxene compositions of neoblasts, porphyroclast cores and rims, intermediate composition, impregnated opx associated with olivine, and opx corroding porphyroclastic cpx

	Mylonite UMB				Mylonite									Proto-mylonite			
Sample:	L187d				L04				L104					L112			
	neoblast $n=4$	rim $n=2$	core $n=4$	imp (cpx) $n=2$	neoblast $n=4$	rim $n=2$	core $n=3$	imp (ol) $n=6$	neoblast $n=5$	rim $n=3$	core $n=3$	imp (ol)r $n=2$	imp (ol)c $n=3$	neoblast $n=2$	rim $n=2$	core $n=3$	imp(ol) $n=3$
wt %																	
SiO_2	57·5(2)	56·4(3)	55·0(1)	54·4(4)	57·5 (4)	56·9(1)	54·2(2)	57·0(3)	57·1(2)	56·8(3)	54·6(1)	56·5(0)	56·2(1)	56·7(4)	56·3(5)	54·8(2)	55·7(3)
TiO_2	0·13(3)	0·16(5)	0·25(2)	0·19(1)	0·19(3)	0·18(5)	0·14(3)	0·18(1)	0·23(2)	0·20(3)	0·19(4)	0·23(4)	0·27(3)	0·23(2)	0·22(1)	0·23(1)	0·24(2)
Al_2O_3	0·92(24)	2·2(2)	3·9(2)	5·0(9)	1·2(3)	1·1(1)	4·96(8)	1·4(2)	1·7(3)	1·8(3)	4·6(1)	2·0(1)	2·5(1)	1·5(5)	1·6(6)	3·88(8)	2·6(4)
Cr_2O_3	0·12(3)	0·35(6)	0·76(1)	0·71(7)	0·24(7)	0·18(1)	0·78(4)	0·22(4)	0·34(8)	0·40(12)	0·84(7)	0·31(08)	0·47(2)	0·28(2)	0·32(16)	0·77(5)	0·57(8)
Fe_2O_3	1·1(3)	0·80(21)	1·2(4)	0·91(59)	1·4(4)	0·21(3)	0·80(44)	0·13(28)	1·1(4)	0·84(58)	1·2(6)	1·6(3)	1·3(1)	0·58(18)	<0·01	<0·01	0·19(23)
FeO	5·9(2)	6·2(5)	5·8(1)	6·1(6)	5·4(3)	6·4(1)	5·87(36)	6·27(31)	5·9(3)	6·2(8)	5·7(4)	5·6(3)	5·7(2)	6·0(5)	6·6(2)	6·5(2)	6·5(2)
MnO	0·20(3)	0·19(1)	0·10(3)	0·18(0)	0·16(2)	0·16(7)	0·11(4)	0·18(1)	0·17(1)	0·19(5)	0·16(2)	0·15(1)	0·14(1)	0·17(6)	0·17(4)	0·15(4)	0·16(2)
NiO	0·06(3)	0·08(2)	0·10(1)	0·11(4)	0·05(3)	0·04(2)	0·13(3)	0·07(2)	0·09(1)	—	—	0·07(4)	0·08(3)	0·09(2)	0·12(6)	0·12(3)	0·09(3)
MgO	34·9(2)	34·1(0)	33·2(1)	32·6(6)	35·1(2)	34·2(1)	32·5(2)	34·2(1)	34·5(1)	34·2(6)	32·9(2)	34·4(1)	34·1(0)	34·1(5)	33·4(5)	32·3(2)	33·2(3)
CaO	0·39(5)	0·35(1)	0·52(2)	0·47(1)	0·51(12)	0·44(8)	0·65(3)	0·45(4)	0·58(5)	0·45(9)	0·65(8)	0·54(2)	0·61(3)	0·57(4)	0·64(10)	0·87(6)	0·58(4)
Na_2O	0·01(1)	0·01(1)	0·02(2)	0·03(1)	0·02(1)	0·01(1)	0·03(2)	0·01(1)	0·01(1)	0·01(1)	0·03(1)	0·02(3)	0·02(1)	0·02(0)	0·02(3)	0·02(1)	0·01(1)
Total	101·1(4)	100·8(4)	101·2(4)	100·6(2)	101·8(2)	99·8(3)	100·1(1)	100·1(3)	101·7(2)	101·1(3)	101·0(3)	101·4(2)	101·3(3)	100·2(1)	99·3(1)	99·7(4)	99·8(6)
Mg-no.	0·902	0·899	0·897	0·895	0·905	0·903	0·899	0·905	0·911	0·907	0·910	0·915	0·913	0·903	0·901	0·898	0·898
Cr-no.	0·080	0·095	0·116	0·087	0·116	0·101	0·095	0·901	0·117	0·129	0·109	0·096	0·115	0·109	0·116	0·117	0·129

	Proto-mylonite					PFG							Porphyroclastic central			
Sample:	La2002-05					L09			L110				L13			
	neoblast $n=4$	rim $n=2$	plateau $n=3$	core $n=4$	imp (ol) $n=3$	neoblast $n=3$	rim $n=2$	core $n=5$	neoblast $n=3$	rim $n=2$	core $n=4$	imp (ol) $n=5$	rim $n=3$	core $n=4$	imp (ol) $n=5$	imp (cpx) $n=5$
wt %																
SiO_2	57·0(6)	56·7(2)	55·6(1)	55·0(1)	56·0(1)	56·2(1)	56·9(2)	55·1(3)	56·8(1)	56·7(2)	55·5(1)	55·5(5)	56·7(2)	55·4(2)	56·3(4)	55·1(3)
TiO_2	0·20(4)	0·23(0)	0·25(1)	0·19(1)	0·27(2)	0·23(2)	0·16(8)	0·22(3)	0·21(5)	0·24(2)	0·25(3)	0·23(2)	0·31(2)	0·25(3)	0·33(3)	0·26(3)
Al_2O_3	1·4(4)	1·6(1)	3·2(1)	3·84(2)	2·4(1)	2·7(1)	1·94(6)	4·12(17)	1·6(3)	1·8(1)	3·1(1)	2·6(2)	2·1(2)	3·28(6)	2·3(5)	3·8(2)

(continued)

Table 3: Continued

	Proto-mylonite					PFG							Porphyroclastic central			
Sample:	La2002-05					L09			L110				L13			
	neoblast	rim	plateau	core	imp (ol)	neoblast	rim	core	neoblast	rim	core	imp (ol)	rim	core	imp (ol)	imp (cpx)
	$n = 4$	$n = 2$	$n = 3$	$n = 4$	$n = 3$	$n = 3$	$n = 2$	$n = 5$	$n = 3$	$n = 2$	$n = 4$	$n = 5$	$n = 3$	$n = 4$	$n = 5$	$n = 5$
Cr_2O_3	0·28(12)	0·35(1)	0·64(6)	0·77(2)	0·48(4)	0·48(5)	0·44(14)	0·81(6)	0·35(11)	0·47(5)	0·70(4)	0·59(3)	0·47(2)	0·70(2)	0·54(4)	0·89(12)
Fe_2O_3	0·50(3)	1·0(1·2)	0·98(20)	1·0(2)	0·90(20)	1·1(4)	0·64(47)	0·47(36)	0·60(52)	<0·01	<0·01	0·84(17)	<0·01	0·27(25)	0·99(29)	1·4(2)
FeO	6·5(1)	5·8(9)	6·0(2)	5·9(2)	6·1(2)	6·0(4)	6·16(6)	6·32(23)	6·5(2)	5·1(5)	5·4(1)	6·1(3)	6·9(1)	7·0(2)	6·1(2)	6·2(1)
MnO	0·16(1)	0·17(1)	0·15(2)	0·14(4)	0·15(6)	0·17(3)	0·14(1)	0·15(4)	0·17(3)	0·10(4)	0·13(4)	0·13(7)	0·18(5)	0·13(3)	0·18(1)	0·18(5)
NiO	0·07(1)	0·11(4)	0·09(1)	0·10(2)	0·08(1)	0·08(3)	0·08(1)	0·07(1)	0·07(3)	0·06(1)	0·08(2)	0·08(2)	0·10(0)	0·08(2)	0·07(3)	0·04(1)
MgO	34·1(5)	34·4(3)	33·3(2)	32·9(1)	33·5(2)	33·7(3)	34·3(2)	32·9(2)	33·9(3)	33·4(2)	32·7(1)	32·8(5)	33·31(6)	32·7(1)	33·6(4)	32·8(4)
CaO	0·58(10)	0·58(1)	0·80(6)	0·85(2)	0·86(6)	0·79(6)	0·50(11)	0·64(18)	0·50(9)	0·78(16)	0·78(9)	1·25(71)	0·69(13)	0·70(5)	0·92(18)	0·82(23)
Na_2O	0·01(1)	0·01(1)	0·02(1)	0·01(1)	0·02(2)	0·02(2)	0·03(3)	0·01(1)	0·01(1)	0·03(1)	0·02(1)	0·05(2)	0·02(1)	0·03(1)	0·03(2)	0·02(1)
K_2O	<0·01	<0·01	<0·01	0·01(1)	<0·01	<0·01	<0·01	<0·01	0·02(2)	0·01(1)	0·01(1)	0·01(1)	<0·01	0·01(1)	0·02(1)	0·01(0)
Total	100·8(3)	100·8(4)	101·0(1)	100·6(1)	100·7(2)	101·4(4)	101·2(1)	100·8(1)	100·7(2)	98·6(2)	98·7(3)	100·3(7)	100·7(7)	100·5(2)	101·3(3)	101·5(3)
Mg-no.	0·898	0·903	0·897	0·898	0·897	0·897	0·902	0·898	0·896	0·921	0·916	0·896	0·895	0·890	0·896	0·889
Cr-no.	0·121	0·129	0·117	0·119	0·118	0·109	0·133	0·116	0·130	0·150	0·130	0·133	0·131	0·125	0·140	0·136

	Porphyroclastic central																
Sample:	L42			L147						L241					L147		
	rim	core	imp (ol)	coarse	rim	plateau	Core	imp (ol)c	imp (ol)r	neoblast	rim	plateau	core	imp (ol)	plateau	core	imp (ol)c
	$n=2$	$n=2$	$n=4$	$n=1$	$n=3$	$n=4$	$n=2$	$n=4$	$n=2$	$n=3$	$n=3$	$n=4$	$n=4$	$n=7$	$n=4$	$n=2$	$n=4$
wt %																	
SiO_2	56·5(3)	54·0(4)	54·8(6)	54·8	55·1(3)	54·4(2)	55·7(1)	55·5(1)	56·4(1)	56·4(4)	56·2(3)	55·3(2)	54·9(2)	56·7(7)	54·4(2)	55·7(1)	55·5(1)
TiO_2	0·22(3)	0·17(7)	0·16(2)	0·28	0·24(1)	0·21(1)	0·27(1)	0·29(2)	0·25(1)	0·19(5)	0·19(4)	0·22(1)	0·19(1)	0·19(8)	0·21(1)	0·27(1)	0·29(2)
Al_2O_3	1·4(4)	4·2(0)	2·9(8)	3·0	1·30(5)	1·68(1)	3·8(3)	2·6(3)	1·7(3)	1·8(4)	2·4(2)	3·4(1)	4·1(0)	1·8(6)	1·68(1)	3·8(3)	2·6(3)
Cr_2O_3	0·33(6)	0·89(8)	0·81(12)	0·69	0·58(5)	0·75(2)	0·80(7)	0·59(8)	0·29(6)	0·30(2)	0·57(2)	0·72(3)	0·79(3)	0·35(16)	0·75(2)	0·80(7)	0·59(8)
Fe_2O_3	0·48(68)	2·0(1·6)	1·9(2)	0·02	<0·01	0·59(24)	0·54(8)	0·24(45)	0·00	1·8(3)	1·0(2)	1·5(2)	1·5(4)	1·0(4)	0·59(24)	0·54(8)	0·24(45)
FeO	6·4(1)	4·4(1·3)	4·6(3)	6·6	6·8(1)	6·2(2)	6·3(0)	6·5(1)	6·62(4)	5·32(0)	6·1(2)	5·6(2)	5·6(4)	6·1(2)	6·2(2)	6·3(0)	6·5(1)
MnO	0·21(6)	0·19(1)	0·17(0)	0·19	0·16(2)	0·14(3)	0·18(4)	0·16(3)	0·13(1)	0·18(3)	0·15(2)	0·16(3)	0·17(4)	0·18(4)	0·14(3)	0·18(4)	0·16(3)
NiO	0·08(3)	0·10(3)	0·10(1)	0·08	0·08(2)	0·10(1)	0·13(4)	0·06(2)	0·07(5)	0·08(2)	0·09(1)	0·11(3)	0·12(3)	0·08(3)	0·10(1)	0·13(4)	0·06(2)
MgO	33·9(1)	33·1(7)	33·4(3)	32·3	32·7(2)	32·3(1)	33·3(3)	32·8(2)	33·5(1)	34·4(3)	33·9(1)	33·4(1)	33·1(2)	34·1(5)	32·3(1)	33·3(3)	32·8(2)
CaO	0·45(26)	0·66(18)	0·84(4)	0·94	0·72(8)	0·88(12)	0·65(8)	0·80(9)	0·62(1)	0·52(15)	0·54(4)	0·66(6)	0·60(4)	0·62(21)	0·88(12)	0·65(8)	0·80(9)

Na_2O	0·02(1)	0·03(0)	0·02(1)	0·03	0·01(1)	0·01(1)	0·02(1)	0·03(1)	0·01(1)	0·01(1)	0·01(1)	0·02(1)	0·01(1)	0·02(1)	0·01(1)	0·02(1)	0·03(1)
K_2O	0·01(1)	0·01(1)	0·01(0)	<0·01	0·01(1)	0·01(1)	0·02(3)	0·00(1)	0·03(1)	<0·01	0·01(2)	0·01(1)	0·01(2)	<0·01	0·01(1)	0·02(3)	0·00(1)
Total	100·0(2)	99·8(6)	99·6(0)	99·01	97·7(4)	97·2(3)	101·7(0)	99·6(5)	99·6(6)	101·0(5)	101·1(1)	101·1(3)	101·0(4)	101·1(2)	97·2(3)	101·7(0)	99·6(5)
Mg-no.	0·899	0·907	0·907	0·897	0·896	0·897	0·898	0·897	0·900	0·900	0·898	0·897	0·897	0·898	0·897	0·898	0·897
Cr-no.	0·136	0·126	0·157	0·132	0·232	0·230	0·124	0·133	0·105	0·102	0·139	0·123	0·115	0·114	0·230	0·124	0·133

	Porphyroclastic central						Porphyroclastic north								
Sample:	L147	L241					W2				L195				
	imp (ol)r	neoblast	rim	plateau	core	imp (ol)	neoblast	rim	core	imp (ol)	rim	core	imp (cpx)	imp (ol)c	imp (ol)r
	$n=2$	$n=3$	$n=3$	$n=4$	$n=4$	$n=7$	$n=1$	$n=4$	$n=2$	$n=4$	$n=5$	$n=5$	$n=5$	$n=6$	$n=5$
wt %															
SiO_2	56·4(1)	56·4(4)	56·2(3)	55·3(2)	54·9(2)	56·7(7)	56·39	55·5(4)	54·1(2)	56·0(6)	56·2(5)	54·9(3)	53·7(3)	56·5(4)	56·5(8)
TiO_2	0·25(1)	0·19(5)	0·19(4)	0·22(1)	0·19(1)	0·19(8)	0·19	0·19(3)	0·13(0)	0·19(5)	0·12(4)	0·13(3)	0·07(2)	0·15(1)	0·14(2)
Al_2O_3	1·7(3)	1·8(4)	2·4(2)	3·4(1)	4·1(0)	1·8(6)	2·15	2·4(3)	4·8(6)	2·1(6)	2·5(3)	4·5(1)	6·2(3)	2·4(5)	2·2(6)
Cr_2O_3	0·29(6)	0·30(2)	0·57(2)	0·72(3)	0·79(3)	0·35(16)	0·44	0·51(4)	0·83(2)	0·32(11)	0·55(7)	1·0(8)	0·86(8)	0·50(12)	0·49(21)
Fe_2O_3	0·00	1·8(3)	1·0(2)	1·5(2)	1·5(4)	1·0(4)	0·18	0·63(34)	0·85(54)	0·16(19)	0·04(6)	0·25(37)	0·26(34)	<0·01	0·41(57)
FeO	6·62(4)	5·32(0)	6·1(2)	5·6(2)	5·6(4)	6·1(2)	6·34	6·0(4)	5·6(5)	6·5(2)	5·8(2)	5·6(3)	6·0(4)	5·9(0)	5·5(6)
MnO	0·13(1)	0·18(3)	0·15(2)	0·16(3)	0·17(4)	0·18(4)	0·15	0·15(1)	0·15(2)	0·16(1)	0·16(1)	0·15(2)	0·16(1)	0·17(2)	0·16(0)
NiO	0·07(5)	0·08(2)	0·09(1)	0·11(3)	0·12(3)	0·08(3)	0·09	0·08(2)	0·08(2)	0·07(1)	0·06(3)	0·05(4)	0·10(1)	0·09(2)	0·08(2)
MgO	33·5(1)	34·4(3)	33·9(1)	33·4(1)	33·1(2)	34·1(5)	33·80	33·2(2)	32·4(1)	33·3(5)	33·7(3)	32·7(7)	32·1(3)	33·8(2)	33·9(5)
CaO	0·62(1)	0·52(15)	0·54(4)	0·66(6)	0·60(4)	0·62(21)	0·57	0·7(1)	0·84(13)	0·67(22)	0·70(10)	0·78(9)	0·55(11)	0·76(12)	0·74(10)
Na_2O	0·01(1)	0·01(1)	0·01(1)	0·02(1)	0·01(1)	0·02(1)	0·01	0·01(1)	0·03(2)	0·01(1)	0·01(1)	0·01(1)	0·02(1)	0·02(0)	0·03(1)
K_2O	0·03(1)	<0·01	0·01(2)	0·01(1)	0·01(2)	<0·01	<0·01	<0·01	<0·01	<0·01	0·01(1)	<0·01	0·01(0)	0·01(0)	0·01(0)
Total	99·6(6)	101·0(5)	101·1(1)	101·1(3)	101·0(4)	101·1(2)	100·31	99·4(3)	99·7(3)	99·5(1)	99·9(3)	100·1(4)	100·1(2)	100·2(1)	100·2(4)
Mg-no.	0·900	0·900	0·898	0·897	0·897	0·898	0·903	0·900	0·902	0·899	0·912	0·909	0·902	0·911	0·912
Cr-no.	0·105	0·102	0·139	0·123	0·115	0·114	0·120	0·123	0·104	0·096	0·126	0·131	0·085	0·124	0·131

UMB, ultra-mylonite bands; PFG, porphyroclastic fine-grained. Plateau, intermediate composition; imp (ol), impregnated opx associated with olivine; imp (cpx), opx corroding porphyroclastic cpx; c, core; r, rim; *n*, number of analyses. Units in parentheses indicate standard deviation from average analysis, and should be read as $56{\cdot}6 \pm 0{\cdot}4$.

Table 4: Olivine composition of neoblasts, and porphyroclast cores and rims

	Mylonite UMB			Mylonite				Proto-mylonite				PFG			
Sample:	L187d			L04		L104		L112		La2002-5		L09		L110	
	neoblast	round neo.	core	neoblast	core	neoblast	core	neoblast	core	neoblast	core	neoblast	core	neoblast	core
	$n=4$	$n=3$	$n=2$	$n=5$	$n=3$	$n=4$	$n=3$	$n=4$	$n=6$	$n=3$	$n=2$	$n=3$	$n=6$	$n=2$	$n=4$
wt %															
SiO_2	41·5(1)	40·8(1)	40·9(1)	41·5(2)	40·9(3)	40·9(2)	41·1(0)	40·9(1)	40·8(2)	41·1(3)	40·9(2)	41·3(2)	40·6(2)	41·0(2)	40·9(2)
TiO_2	0·02(1)	0·01(1)	0·02(2)	0·01(1)	0·01(2)	0·01(1)	0·01(1)	0·01(1)	0·04(7)	0·01(1)	0·02(2)	0·02(2)	0·00(1)	0·02(1)	0·01(1)
Al_2O_3	0·01(1)	0·01(1)	0·01(1)	0·38(81)	<0·01	0·01(1)	0·01(1)	<0·01	<0·01	0·01(1)	0·01(1)	0·00(1)	<0·01	0·01(1)	0·01(1)
Cr_2O_3	0·02(2)	0·01(2)	0·01(1)	0·03(3)	0·01(1)	<0·01	0·01(2)	0·04(4)	0·02(2)	0·07(9)	0·02(0)	0·06(5)	0·02(2)	0·02(3)	0·01(2)
FeO	8·2(4)	10·0(2)	10·3(2)	9·41(22)	9·5(5)	11·5(8)	10·9(3)	9·7(2)	9·7(2)	9·6(3)	10·2(2)	9·8(2)	9·7(2)	10·3(6)	10·2(1)
MnO	0·05(1)	0·15(3)	0·19(9)	0·14(4)	0·16(2)	0·26(7)	0·20(2)	0·17(4)	0·18(4)	0·14(2)	0·11(1)	0·15(3)	0·16(1)	0·12(7)	0·17(4)
NiO	0·40(4)	0·37(2)	0·39(3)	0·38(5)	0·36(4)	0·26(10)	0·35(2)	0·38(1)	0·37(1)	0·36(4)	0·38(6)	0·37(1)	0·38(2)	0·38(0)	0·37(3)
MgO	51·2(3)	49·4(1)	49·6(2)	49·9(8)	49·5(5)	48·3(6)	48·8(3)	49·0(2)	48·8(4)	49·9(4)	49·2(1)	49·8(2)	49·1(1)	49·1(3)	49·2(2)
CaO	0·10(2)	<0·01	0·03(1)	0·21(28)	0·02(2)	0·01(1)	0·01(1)	0·02(1)	0·03(1)	<0·01	0·05(1)	0·02(1)	0·04(1)	0·07(4)	0·03(0)
Na_2O	0·01(1)	0·01(1)	0·01(1)	0·02(2)	0·01(1)	0·01(1)	0·00(1)	0·01(1)	<0·01	0·01(1)	0·01(1)	0·01(1)	0·00(1)	0·02(2)	0·01(1)
Total	101·5(2)	100·7(2)	101·4(3)	101·93(53)	100·5(4)	101·3(2)	101·4(1)	100·2(3)	100·0(6)	101·2(3)	100·9(1)	101·4(3)	100·0(2)	101·0(0)	100·9(2)
Mg-no.	0·918	0·898	0·896	0·904	0·901	0·883	0·888	0·900	0·900	0·903	0·896	0·901	0·900	0·895	0·895

	Porphyroclastic central				Porphyroclastic north		
Sample:	L13	L42	L147	L241	L195	L195	W2
	core	core	core	neoblast	core	core	core
	$n=2$	$n=3$	$n=3$	$n=3$	$n=8$	$n=3$	$n=4$
wt %							
SiO_2	41·1(1)	41·0(0)	40·7(0)	40·9(1)	41·0(1)	41·0(2)	40·6(8)
TiO_2	0·01(1)	0·01(1)	<0·01	<0·01	0·01(1)	<0·01	0·01(1)
Al_2O_3	0·01(1)	0·04(6)	<0·01	<0·01	0·01(1)	0·01(1)	0·02(4)
Cr_2O_3	<0·01	0·01(1)	0·01(1)	0·05(5)	0·03(1)	0·01(1)	0·01(1)
FeO	10·9(2)	9·2(8)	10·0(3)	10·0(3)	8·6(1)	10·3(2)	9·57(5)
MnO	0·19(3)	0·16(1)	0·14(2)	0·14(2)	0·14(1)	0·15(2)	0·14(1)
NiO	0·35(1)	0·38(4)	0·35(2)	0·40(4)	0·40(3)	0·40(3)	0·39(2)
MgO	49·1(1)	50·1(13)	48·9(5)	49·6(2)	50·0(3)	48·8(2)	49·15(6)
CaO	0·03(1)	0·05(4)	0·02(1)	0·02(1)	0·03(2)	0·04(2)	0·02(2)
Na_2O	0·01(1)	0·01(1)	<0·01	0·01(1)	0·07(15)	0·01(1)	<0·01
Total	101·73(3)	100·9(3)	100·1(7)	101·1(2)	100·2(4)	100·7(2)	99·9(1)
Mg-no.	0·889	0·907	0·897	0·898	0·912	0·894	0·902

UMB, ultra-mylonite bands; PFG, porphyroclastic fine-grained. Units in parentheses indicate standard deviation from average analysis, and should be read as $56{\cdot}6 \pm 0{\cdot}4$. *n*, number of analyses; Mg-number $= Mg/(Mg + Fe_{tot})$.

coexisting plagioclase), is related to domain I; (2) low Al occurs in domain II (Fig. 11). This translates into systematic temperature differences for the two orthopyroxene populations, if Al-in-opx thermometry is applied (see below).

Spinel

Spinel analyses from all groups from the Lanzo massif cover almost the entire compositional range for abyssal peridotites and indicate substantial variation in TiO_2

Table 5: Spinel composition of neoblasts, and porphyroclast cores and rims

	Mylonite UMB		Mylonite			Proto-mylonite				PFG			
Sample:	L187d		L04		L104	L112		La2002-05		L09		L110	
	neoblast	core	neoblast	core	core	neoblast	core	neoblast	core	neoblast	core	neoblast	core
	n = 4	*n* = 2	*n* = 4	*n* = 4	*n* = 5	*n* = 3	*n* = 2	*n* = 3	*n* = 4	*n* = 6	*n* = 5	*n* = 2	*n* = 3
wt %													
SiO_2	0·03(1)	0·02(2)	0·06(3)	0·02(2)	0·08(15)	0·01(1)	<0·01	0·01(1)	<0·01	0·03(1)	0·01(0)	0·02(1)	<0·01
TiO_2	0·19(11)	0·44(17)	0·39(16)	0·59(5)	0·28(16)	0·57(22)	1·15(73)	0·50(8)	0·54(3)	0·40(13)	0·40(4)	0·54(16)	0·97(41)
Al_2O_3	33·1(2·0)	35·1(1·4)	35·6(5·5)	32·0(4)	28·5(1·8)	27·4(4·5)	31·6(5)	27·2(2·3)	31·3(2)	32·7(6·8)	36·76(9)	30·2(2·3)	31·0(4)
Cr_2O_3	29·3(1·4)	27·2(1·3)	26·7(5·7)	29·5(3)	30·6(1·6)	29·5(3·7)	31·3(1)	33·1(2·8)	31·0(2)	28·0(5·9)	27·56(31)	31·0(2·2)	30·4(5)
Fe_2O_3	6·2(6)	6·2(2)	6·0(3)	7·0(1)	7·51(39)	10·2(1·2)	5·6(7)	7·0(3)	6·1(1)	6·5(1·0)	4·97(24)	5·8(0·3)	6·16(15)
FeO	19·0(1·0)	16·9(7)	18·4(2·0)	14·7(2)	23·3(1·0)	23·0(2·2)	16·6(9)	19·5(4)	14·8(1)	19·0(2·5)	14·7(3)	17·4(2·0)	15·9(4)
MnO	0·10(9)	0·11(1)	0·27(2)	0·13(4)	0·46(5)	0·24(9)	0·17(1)	0·16(3)	0·15(1)	0·23(7)	0·16(6)	0·21(4)	0·11(10)
NiO	0·16(2)	0·25(1)	0·23(6)	0·24(1)	0·18(3)	0·19(2)	0·19(2)	0·18(6)	0·22(3)	0·21(4)	0·22(6)	0·15	0·23(7)
MgO	11·7(1·0)	13·3(6)	12·2(1·7)	14·3(2)	8·0(6)	8·4(2·0)	13·7(3)	10·5(6)	14·1(1)	11·3(2·2)	14·0(2)	12·1(1·7)	13·7(2)
CaO	0·03(1)	<0·01	0·03(4)	0·01(1)	<0·01	0·01(1)	<0·01	0·01(1)	0·01(1)	0·01(1)	<0·01	0·01(1)	<0·01
Na_2O	0·01(1)	0·02(1)	—	0·02(2)	—	0·02(2)	0·02(1)	0·01(1)	—	—	—	—	—
K_2O	0·00(1)	<0·01	—	0·00(1)	—	<0·01	<0·01	0·00(1)	—	—	—	—	—
ZnO	0·20(6)	0·25(2)	0·24(5)	0·16(7)	0·4(1)	0·37(10)	0·17(1)	0·32(4)	0·13(10)	0·42(10)	0·18(7)	0·30(10)	0·20(4)
Total	100·0(1·0)	99·8(0)	100·1(6)	98·6(2)	99·4(1)	99·9(6)	100·5(0)	97·8(3)	98·4(3)	98·8(4)	99·9(4)	97·6(2)	98·6(3)
Mg-no.	0·465	0·519	0·54	0·63	0·37	0·32	0·54	0·426	0·561	0·45	0·59	0·49	0·54
Cr-no.	0·372	0·342	0·36	0·39	0·42	0·42	0·40	0·450	0·400	0·40	0·33	0·41	0·40

	Porphyroclastic central						Porphyroclastic north		
Sample:	L13	L42		L147	L241		W2	L195	
	core	neoblast	core	core	neoblast	Core	core	rim	core
	n = 2	*n* = 2	*n* = 3	*n* = 2	*n* = 3	*n* = 3	*n* = 4	*n* = 4	*n* = 4
wt %									
SiO_2	0·02(2)	0·04(1)	0·02(1)	0·05(1)	0·05(3)	0·03(2)	0·02(1)	0·03(1)	0·02(1)
TiO_2	0·64(2)	0·66(2)	0·62(4)	0·55(6)	0·29(2)	0·55(17)	0·43(24)	0·39(4)	0·38(7)
Al_2O_3	25·8(0)	28·9(3)	28·5(6)	30·7(2)	33·5(1·3)	33·5(4)	28·5(9)	30·7(5)	32·8(1·0)
Cr_2O_3	31·5(6)	33·0(1·2)	34·1(1·2)	31·1(4)	27·9(1·8)	29·3(5)	32·8(5)	31·5(7)	30·4(3)
Fe_2O_3	9·47(58)	6·1(1)	6·5(7)	6·6(2)	6·2(2)	7·1(2)	7·4(9)	5·8(4)	5·9(5)
FeO	23·0(6)	17·0(2)	18·0(1·2)	18·3(4)	19·0(2)	15·3(1)	22·0(1·1)	20·7(1·6)	17·1(2·7)
MnO	0·14(2)	0·73(2)	0·68(3)	0·17(6)	0·20(5)	0·11(6)	0·77(4)	0·79(7)	0·68(06)
NiO	0·20(4)	0·17(4)	0·20(2)	0·20(3)	0·20(2)	0·28(2)	0·17(4)	0·20(3)	0·20(3)
MgO	8·2(2)	12·2(3)	11·9(8)	12·0(5)	11·5(2)	14·5(1)	8·7(1·3)	9·8(1·5)	12·7(1·8)
CaO	0·01(1)	0·01(1)	0·01(1)	0·02(1)	0·02(1)	0·00(1)	0·01(1)	—	—
Na_2O	0·03(2)	<0·01	<0·01	0·02(2)	0·01(2)	0·01(1)	<0·01	—	—
K_2O	0·02(0)	<0·01	<0·01	<0·01	<0·01	0·01(1)	<0·01	—	—
ZnO	—	0·39(6)	0·19(20)	0·23(1)	0·29(7)	0·20(4)	1·4(7)	0·76(71)	0·21(9)
Total	99·4(4)	99·2(9)	100·7(5)	99·9(5)	99·2(2)	100·8(2)	100·7(3)	100·8(6)	100·4(5)

(continued)

Table 5: Continued

	Porphyroclastic central						Porphyroclastic north		
Sample:	L13	L42		L147	L241		W2	L195	
	core	neoblast	core	core	neoblast	Core	core	rim	core
	$n=2$	$n=2$	$n=3$	$n=2$	$n=3$	$n=3$	$n=4$	$n=4$	$n=4$
Mg-no.	0·011	0·50	0·48	0·47	0·010	0·550	0·043	0·41	0·51
Cr-no.	0·451	0·43	0·44	0·40	0·359	0·370	0·436	0·41	0·38

UMB, ultra-mylonite bands; PFG, porphyroclastic fine-grained. Units in parentheses indicate standard deviation from average analysis, and should be read as $56{\cdot}6 \pm 0{\cdot}4$. *n*, number of analyses; Mg-number $= Mg/(Mg + Fe_{tot})$; Cr-number $= Cr/(Cr + Al)$.

Table 6: Plagioclase compositions

	Mylonite		Proto-mylonite		PFG	P
Sample:	L04		L112	La02-5	L09	L241
	neoblast	core				
	n = 7	n = 11	n = 8	n = 7	n = 12	n = 12
wt %						
SiO_2	49·5(9)	50·4(4)	49·9(6)	48·8(4)	49·6(7)	48·5(5)
TiO_2	0·05(3)	0·03(1)	—	—	—	—
Al_2O_3	33·0(3)	33·1(2)	32·6(5)	33·0(4)	33·2(5)	33·6(4)
Fe_2O_3	<0·01	0·10(5)	0·08(6)	0·12(6)	0·16(13)	0·13(5)
FeO	0·12(3)	0·01(2)	0·04(6)	<0·01	0·02(4)	0·01(3)
MnO	<0·01	<0·01	—	—	—	—
MgO	<0·01	<0·01	—	—	—	—
CaO	15·2(7)	15·3(3)	14·4(4)	15·7(4)	14·9(5)	15·6(4)
Na_2O	2·7(4)	3·1(2)	3·3(2)	2·7(2)	3·07(31)	2·6(2)
K_2O	<0·01	0·01(1)	0·01(1)	0·01(1)	0·01(1)	0·01(1)
Total	100·6(4)	101·9(7)	100·3(9)	100·4(3)	100·9(3)	100·5(3)
An	0·750	0·730	0·730	0·760	0·730	0·770

n, number of analyses; PFG, porphyroclastic fine-grained; P, porphyroclastic. Units in parentheses indicate standard deviation from average analysis, and should be read as $56{\cdot}6 \pm 0{\cdot}4$.

Cr-number and Mg-number (Fig. 12). The majority of spinel neoblasts and porphyroclasts contain between 0·18 and 1 wt % of TiO_2 although exceptionally high values up to 5·1 wt % were found in some samples. These values are much higher than those generally found in spinel peridotites (Dick & Bullen, 1984; Hellebrand *et al.*, 2001; Hellebrand & Snow, 2003), but TiO_2 up to 1 wt % is fairly common for plagioclase peridotites (Cannat *et al.*, 1997*b*; Dick, 1989). The enrichment and extreme variation of TiO_2 in spinel contrasts with the rather small variations in olivine Mg-number (88–91). Surprisingly, within a single sample, the spinel composition covers almost the entire range of abyssal peridotite (Fig. 12). If the spinel compositions are plotted according to their respective microstructural group described above, we see that the variability is correlated with the degree of deformation. The largest variations are observed in the porphyroclastic peridotites from the central body, whereas spinel composition in strongly deformed rocks (mylonite and mylonite with ultra-mylonite bands) is more homogeneous in terms

Table 7: Amphibole composition in plagioclase peridotite

	M-UMB	Mylonite	Proto-mylonite		PFG		Porphyroclastic central		
Sample:	L187d	L04	L112	La2002-5	L09	L110	L13	L147	L241
	$n=4$	$n=3$	$n=5$	$n=3$	$n=5$	$n=4$	$n=3$	$n=7$	$n=5$
wt %									
SiO_2	44·4(3)	43·0(6)	42·3(4)	43·3(1)	43·2(3)	42·7(4)	43·9(5)	42·5(5)	42·5(7)
TiO_2	3·0(3)	4·3(5)	4·2(2)	3·6(4)	2·7(2)	4·1(2)	3·4(7)	3·5(4)	3·3(6)
Al_2O_3	12·1(3)	13·2(8)	11·5(3)	11·5(4)	11·8(4)	11·8(2)	12·2(4)	13·5(5)	12·0(4)
Cr_2O_3	1·21(2)	1·53(2)	1·54(2)	1·78(4)	1·82(2)	1·61(2)	1·52(1)	1·39(2)	1·41(2)
Fe_2O_3	0·00	<0·01	0·00	0·00	<0·01	—	0·00	0·00	0·00
FeO	3·8(2)	4·3(5)	4·3(1)	4·2(2)	4·9(2)	4·5(2)	5·1(5)	4·1(1)	5·0(2)
MnO	0·07(2)	0·04(2)	0·04(3)	0·10(4)	0·05(2)	0·06(2)	0·06(4)	0·08(1)	0·05(3)
NiO	0·08(1)	—	0·1(3)	0·10(1)	0·10(3)	0·09(2)	—	0·09(2)	0·10(3)
MgO	17·3(2)	17·0(2)	16·6(1)	16·9(3)	17·1(2)	16·6(2)	16·9(1)	16·4(4)	17·4(5)
CaO	12·3(3)	12·1(1)	12·4(2)	12·3(1)	12·3(1)	12·3(3)	12·7(3)	12·4(2)	12·3(3)
Na_2O	3·5(2)	3·7(1)	3·4(1)	3·4(0)	3·3(1)	3·4(2)	3·3(1)	3·6(1)	3·3(1)
K_2O	0·01(1)	0·01(2)	0·01(2)	<0·01	0·00(1)	0·02(2)	0·05(1)	0·01(0)	0·00(1)
H_2O	2·1(1)	2·09(2)	2·0(0)	2·1(0)	2·0(0)	2·0(1)	2·1(0)	2·1(0)	2·1(1)
Total	99·8(6)	101·1(6)	98·4(4)	99·2(3)	99·3(1)	99·2(3)	101·1(3)	99·7(4)	99·3(2)
Mg-no.	0·892	0·875	0·872	0·878	0·861	0·868	0·761	0·876	0·861
Cr-no.	0·064	0·072	0·080	0·095	0·093	0·085	0·074	0·066	0·070

M-UMB, mylonite with ultra-mylonite bands; PFG, porphyroclastic fine-grained. Units in parentheses indicate standard deviation from average analysis.

of TiO_2 and Cr-number, suggesting a faster and more complete equilibration among small grains than in porphyroclastic samples. The spinel compositions from the northern body are homogeneous, suggesting equilibration in the plagioclase facies. The extreme variation of TiO_2 content in spinel cannot be explained by simple fractional crystallization in a closed system (e.g. Villiger *et al.*, 2004), but must be related to large compositional variations of migrating (ephemeral) liquid within a peridotite matrix. TiO_2 contents exceeding 1 wt % are usually associated with the crystallization of spinel in troctolites or olivine gabbros (e.g. Dick & Natland, 1996). However, the extreme variability is not restricted to a particular microstructure. The within-sample variation indicates that equilibrium on a thin-section scale is not attained. This is illustrated in Fig. 13, where two compositional cross-sections from the same sample are shown. BSE images of spinel porphyroclasts show an irregular distribution of dark zones (corresponding to high-Al spinel, maximum 1·8 p.f.u.), surrounding brighter zones (Fig. 13a and b). Such an irregular distribution is best explained by melt–rock reaction. In contrast, there are more regular spinels, with a ± symmetrical inverse zonation, with a core to rim decrease of Al from 1·1 to 0·9 p.f.u., and a corresponding Cr increase from 0·73 to 0·86 p.f.u (Fig. 13c–f). This is compatible with cooling during exhumation of the peridotites (Müntener *et al.*, 2000). This also suggests that once the plagioclase peridotites completely crystallized, exhumation to shallower depths must have been rapid to preserve such disequilibrium chemical compositions.

Olivine

Electron microprobe analyses were performed on cores and rims of large porphyroclasts and neoblasts (Table 4) and show a restricted range of chemical variation with respect to olivine Mg-number [molar $Mg/(Mg + Fe_{tot})$]. Olivine displays uniform Mg-number between 0·89 and 0·905, and NiO between 0·37 and 0·40 wt %. Olivine from one mylonite sample (L104, more serpentinized than L04), displays slightly lower Mg-number (0·89 porphyroclastic core, and 0·88 in neoblasts). Olivine crystals show similar NiO contents in both cores (0·35–0·40 wt %) and neoblasts (0·36–0·40 wt %). However, within one sample NiO shows a slight increase from core to rim (sample L04, 0·36 wt % in core to 0·38 wt % in neoblasts).

Plagioclase

Plagioclase analyses were performed on six samples. The chemical composition of plagioclase is variable and may be influenced by the microstructure; however, most

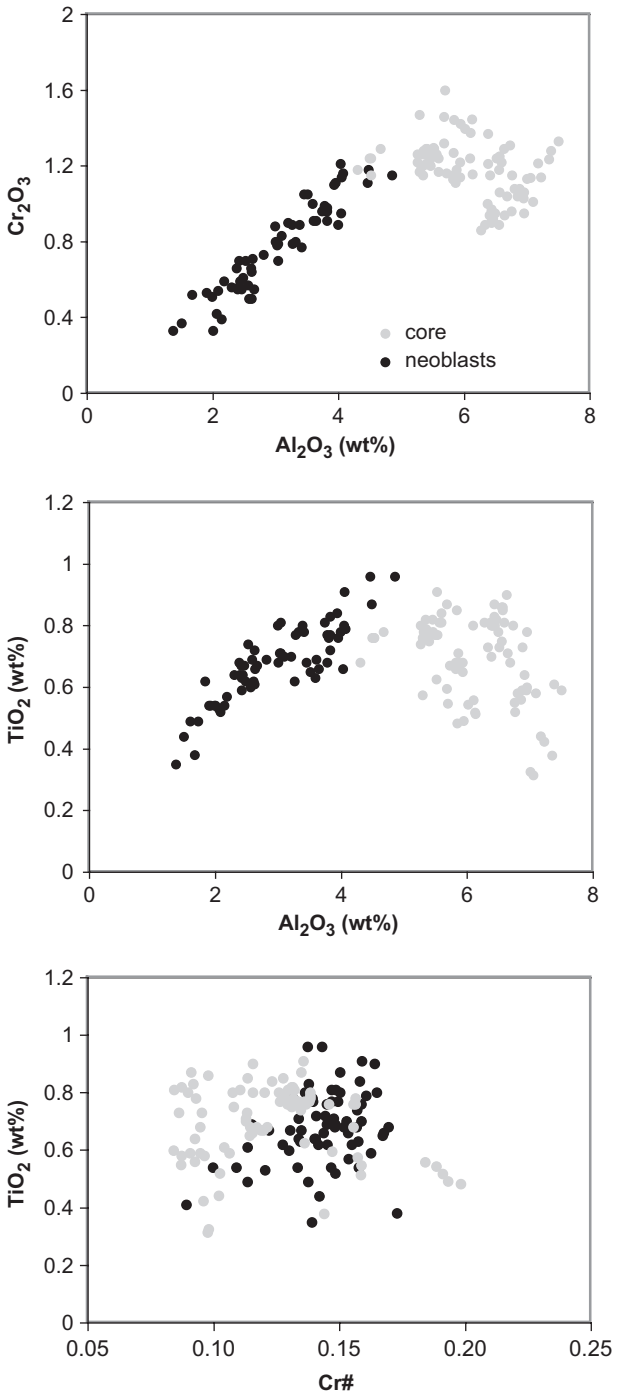

Fig. 8. Clinopyroxene composition from porphyroclasts (grey circles) and neoblasts (black circles). Porphyroclast analyses in 13 samples are from all rock categories (porphyroclastic, PFG, proto-mylonite, mylonite). Neoblast analyses from six samples represent mylonite, proto-mylonite and PFG rocks. The Al content decreases from cores to neoblasts, which is classically observed during the spinel- to plagioclase-facies transition. It should be noted that TiO_2 increases with decreasing Al_2O_3 for the porphyroclastic cpx (negative correlation), whereas for the neoblasts, Cr_2O_3 and TiO_2 correlate positively with Al_2O_3.

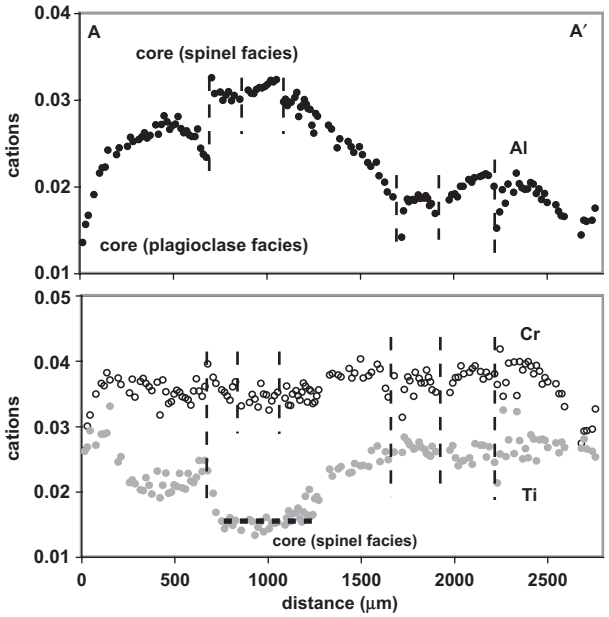

Fig. 9. Representative clinopyroxene compositional variation in terms of Al, Cr, and Ti (atoms per formula unit) (sample L13, porphyroclastic). The core displays the highest Al and lowest Ti content, indicating equilibration in the spinel peridotite facies. Decreasing Al is coupled with increasing Ti, whereas the Cr content shows little variation. The areas indicated by vertical dashed lines display orthopyroxene + plagioclase intergrowth (see location of cross-section in Fig. 7f).

plagioclase compositions vary between An_{75} and An_{80} (Table 6). The major difference is a slightly higher Na_2O content (2·36–4·00 wt %) in the mylonite than in the porphyroclastic samples (e.g. 2·0–3·5 wt % Na_2O, Table 5). Plots of olivine Mg-number vs An in plagioclase (not shown) do not show correlations as in common gabbroic rocks from the oceanic crust (e.g. Dick & Natland, 1996).

Amphibole

Amphiboles are all K-poor Ti-pargasites (Table 7), with TiO_2 contents of 2·7–4·3 wt %, and Cr_2O_3 contents of 1·21–1·82 wt %. Mg-numbers (86·1–89·2) are slightly lower than for coexisting olivine and pyroxenes, with one exception with a significantly lower Mg-number of 76·2. Amphiboles have very low K_2O contents (<0·05 wt %) and are thus different from many mantle amphiboles related to modal metasomatism in ophiolitic peridotites and mantle xenoliths (Vannucci *et al.*, 1995).

THERMOMETRY

A large number of geothermometers have been experimentally and empirically calibrated for upper mantle assemblages. Temperatures calculated in this study are based on the following formulations: (1) the experimental calibration of Brey & Köhler (1990), a thermometer based on

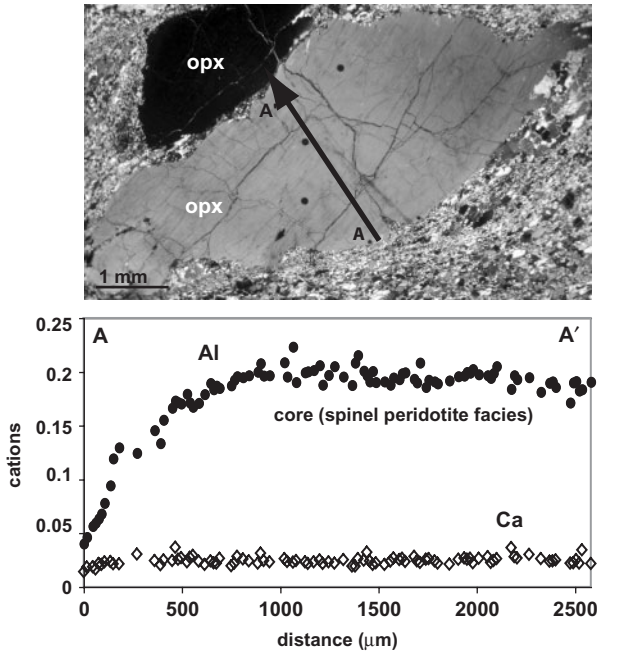

Fig. 10. Compositional zoning of orthopyroxene from a peridotite mylonite (L04). It should be noted that there is a ~1000 μm thick region of decrease of Al towards the rim, whereas Ca shows only a weak zoning within the last 150 μm. At A, the contact with the matrix in the first 250 μm of the opx is abrupt and does not exhibit gradational zoning towards the mylonitic matrix, indicating syndeformational brittle fracturing of the orthopyroxene porphyroclasts. From 250 to 750 μm the zoning is more gradational and represents the transition from spinel to plagioclase peridotite facies. This happens at high temperature and Ca completely equilibrates. The part A′ corresponds to the core of the opx, suggesting that it was broken at the end of the deformation, which did not permit equilibrium with the matrix.

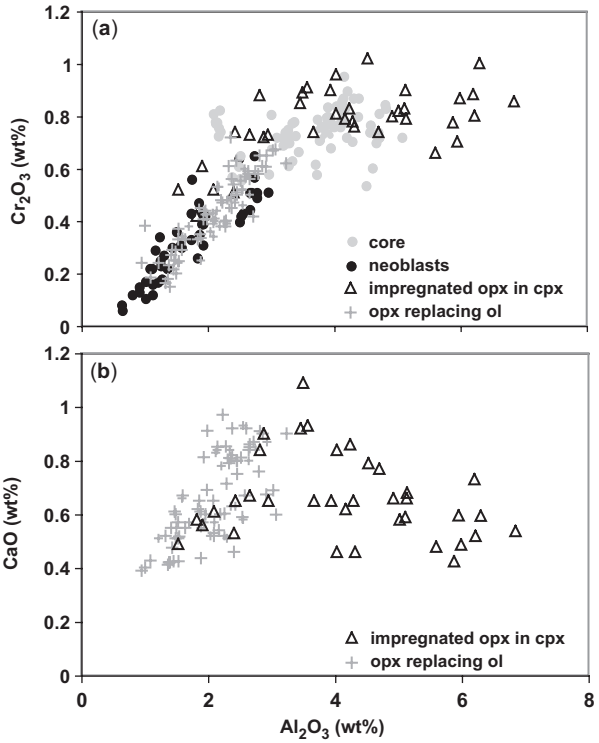

Fig. 11. (a) Al_2O_3 vs Cr_2O_3 of orthopyroxene for porphyroclast cores, neoblasts, orthopyroxene replacing clinopyroxene (domain I), and orthopyroxene replacing olivine (domain II). The lowest Al and Cr contents are from mylonitic neoblasts and some opx from domain II. (b) Al_2O_3 vs CaO for orthopyroxene related to melt–rock reaction processes. It should be noted that orthopyroxene replacing clinopyroxene (domain I) has higher Al_2O_3 contents than orthopyroxene replacing olivine (domain II), indicating that the high Al_2O_3 content is inherited from precursor clinopyroxene. Also, the CaO content in 'reacted' orthopyroxene does not show significant differences between the microstructural sites, indicating some post-reaction thermal equilibration.

coexisting clinopyroxene and orthopyroxene ($T_{2\text{-pyx BK90}}$); (2) the Ca-in-opx thermometer, with opx in equilibrium with clinopyroxene ($T_{\text{Ca-in-opx BK90}}$); (3) the Al and Cr contents in orthopyroxene ($T_{\text{Al,Cr-in-opx WS91}}$) as defined by Witt-Eickschen & Seck (1991); (4) the Fe^{2+}–Mg exchange between olivine and spinel (Ballhaus *et al.*, 1991). Results of the geothermometry calculations are summarized in Table 8. Pressures were assumed to be 1 GPa for cores, implying that equilibration took place in the spinel stability field (Klemme & O'Neill, 2000), and 0·5 GPa for rims and neoblasts (Gasparik, 1987).

The strong Al zoning in clino- and orthopyroxene indicates that bulk equilibration has not been attained. In porphyroclastic orthopyroxene, however, there is a large plateau in terms of Al and diffusion related to cooling has affected the outer 1000 μm only (Fig. 10). Application of the Witt-Eickschen & Seck (1991) thermometer results in relatively homogeneous temperatures for orthopyroxene cores for all structural domains, ranging from 1030 to 1100°C. On average, these temperatures are ~80°C higher than those obtained by the Ca-in-orthopyroxene thermometer of Brey & Köhler (1990). This discrepancy is readily explained by the much faster diffusive equilibration of Ca-in-opx compared with Al-in-opx (Smith *et al.*, 1999), and the tendency of clinopyroxene to preferentially recrystallize, especially in deformed samples such as those from Lanzo. Substantially slower diffusion of Al and Cr compared with Fe, Mg and Ca has also been observed by Ozawa & Takahashi (1995).

In contrast, temperature estimates from orthopyroxene rims preserve a very different thermal history. Applying the Ca-in-opx thermometer of Brey & Köhler (1990), the Ca concentration would correspond to a mean temperature of ~910°C for the porphyroclastic, PFG and protomylonites (Table 8). Mylonites record progressively lower temperatures, reaching ~820°C. Neoblasts provide similar results, with the lowest temperatures recorded by the ultra-mylonitic zone. Independent of the accuracy of the absolute temperature, there is a temperature difference of the order of 150°C for neoblasts across the shear zone.

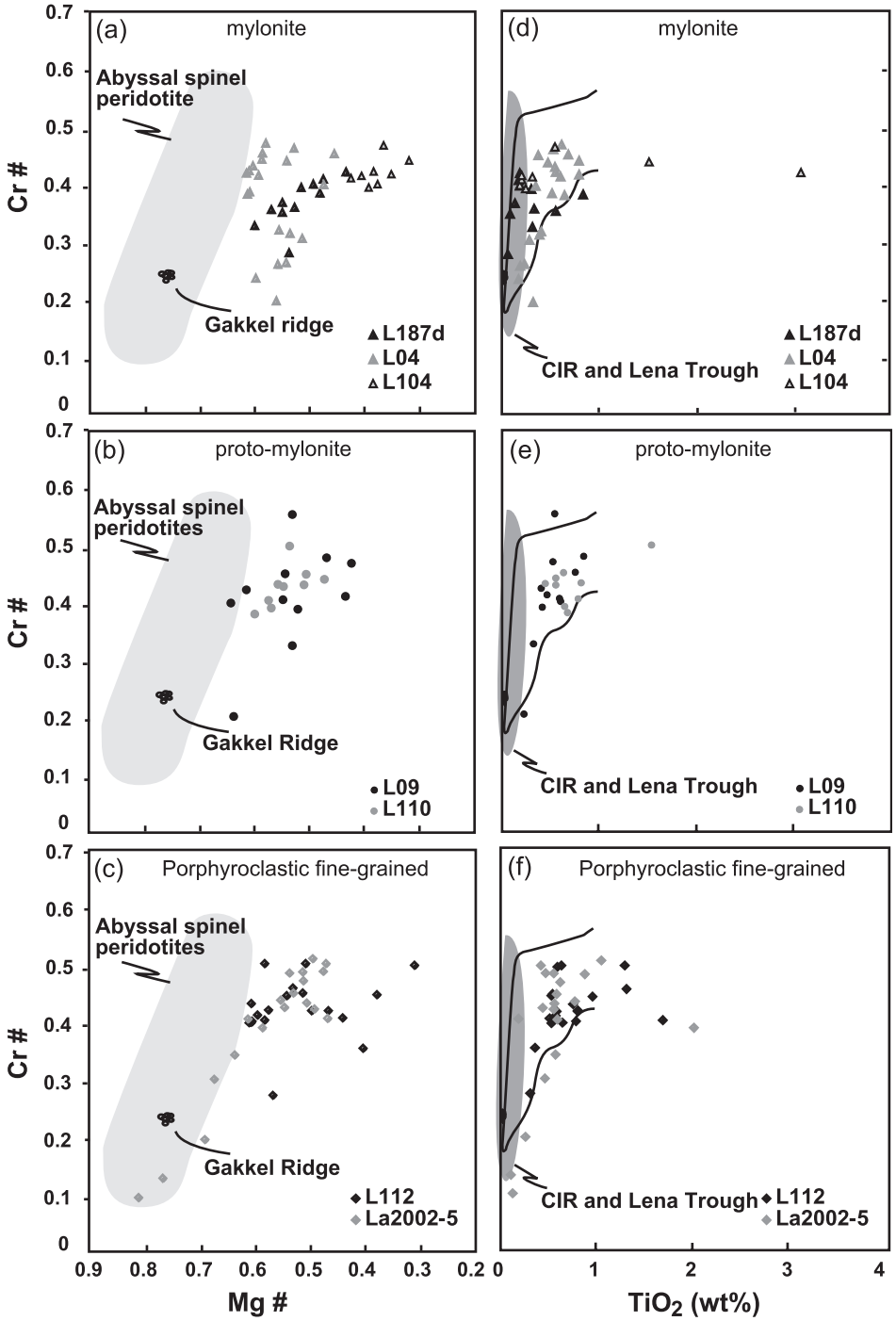

Fig. 12. (a, b, c, g, h) Cr-number vs Mg-number of spinels from the Lanzo shear zone. Cr-number of spinels from the investigated samples varies from 0·1 to 0·6. Most samples plot to the right of the abyssal spinel peridotite field (Hellebrand *et al.*, 2002; Hellebrand & Snow, 2003) consistent with equilibration in the plagioclase peridotite field and probable addition of olivine + plagioclase ± orthopyroxene (Dick & Natland, 1996). (d, e, f, i, j) TiO_2 (wt %) vs Cr-number. CIR (Central Indian Ridge) data are from E. Hellebrand (unpublished data), and Lena Trough data are from Hellebrand & Snow (2003). It should be noted that almost all spinel analyses exceed 0·2 wt% TiO_2. High TiO_2 in spinel is associated with the crystallization of spinel from migrating liquids and is a characteristic feature of Cr-spinel in dunite, troctolite and olivine gabbros (Dick & Natland, 1996; Cannat *et al.*, 1997*a*). It should be noted that the extreme variability of TiO_2 in porphyroclastic and PFG is greatly reduced in proto-mylonites and mylonites, suggesting 'homogenization' of compositional variability during deformation. Also, spinels from the northern body (h, j) display less variation than those from the south.

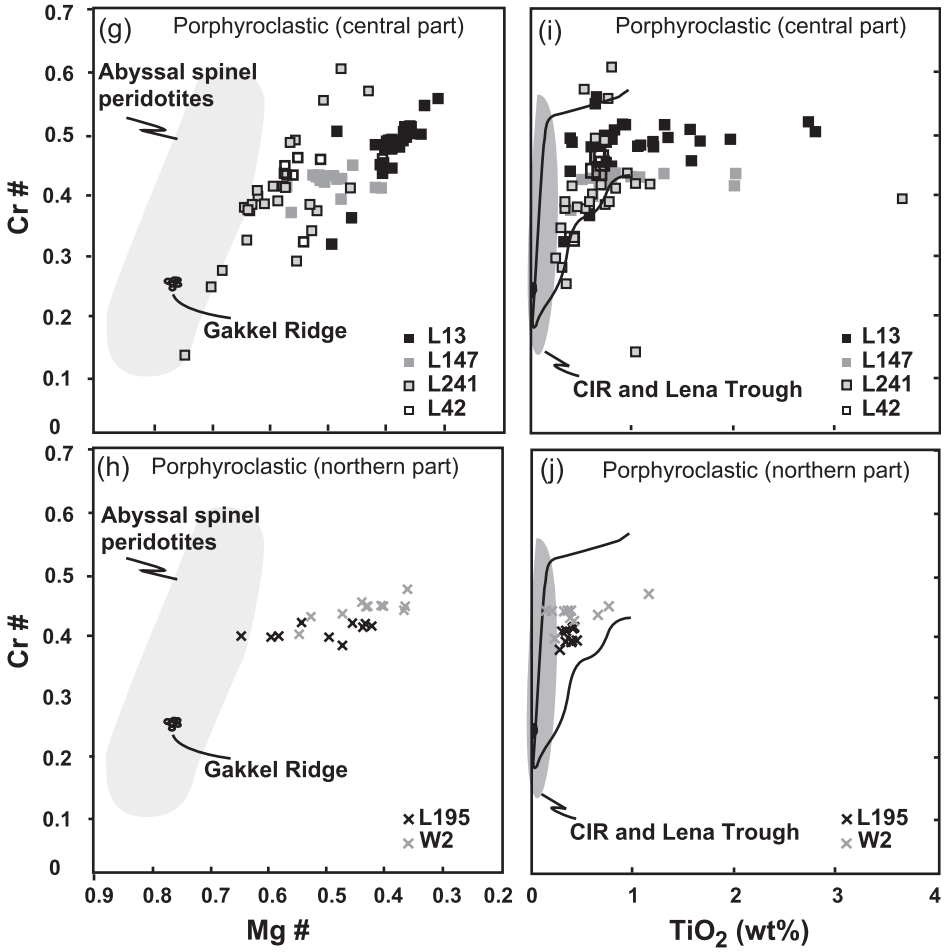

Fig. 12. Continued

The temperature range for all exsolution-free orthopyroxenes related to melt–rock reaction (e.g. domain I and II; see Fig. 7), lies around 950°C ($T_{\text{Al,Cr-in-opx WS91}}$), whereas temperatures obtained by applying the Witt-Eickschen & Seck calibration ($T_{\text{Al,Cr-in-opx WS91}}$) result in 1053 ± 30°C and 890 ± 61 °C for domain I and II, respectively. The temperature difference of ~200°C suggests that full equilibrium was attained in terms of Ca, but not for Al and Cr. The contrasting temperatures obtained by $T_{\text{Al,Cr-in-opx WS91}}$ are artefacts of the orthopyroxene-forming process and are locally controlled by the availability of Al (and Cr). One important observation is that the average Al content of orthopyroxene from domain II exceeds that of the large orthopyroxene porphyroclasts (Fig. 10); this could be an inherited effect from mantle clinopyroxene, which is generally considered to accommodate higher Al and Cr contents than opx (e.g. Brey & Köhler, 1990).

The calculations derived from olivine–spinel geothermometry provide very different results. The highest temperatures are preserved in the porphyroclastic cores from the mylonitic rocks (proto-mylonite and mylonite, 1051 °C and 1136°C, respectively), approaching the conditions obtained from orthopyroxene thermometry ($T_{\text{Al,Cr-in-opx WS91}}$), whereas the calculated values for porphyroclastic fine-grained rocks approach those of Ca-in-opx ($T_{\text{Ca-in-opx BK90}}$). Calculated temperatures for opx neoblast are ~600°C in the ultra-mylonite bands and ~800°C for all other rock types (Table 8).

DISCUSSION

Reactive melt percolation and relation with deformation

Melt–rock interaction is evident in the Lanzo peridotite massif and is observed from hand specimen to grain scale. Early important studies on the Lanzo massif (Boudier, 1972, 1978; Nicolas *et al.*, 1972; Bodinier *et al.*, 1991), described the presence of melt as gabbroic lenses, whereas more recent studies have highlighted melt–rock reaction in the Lanzo peridotite (e.g. Müntener & Piccardo, 2003; Piccardo *et al.*, 2007). Our results focus on the spatial relationships of deformation and distribution of textures

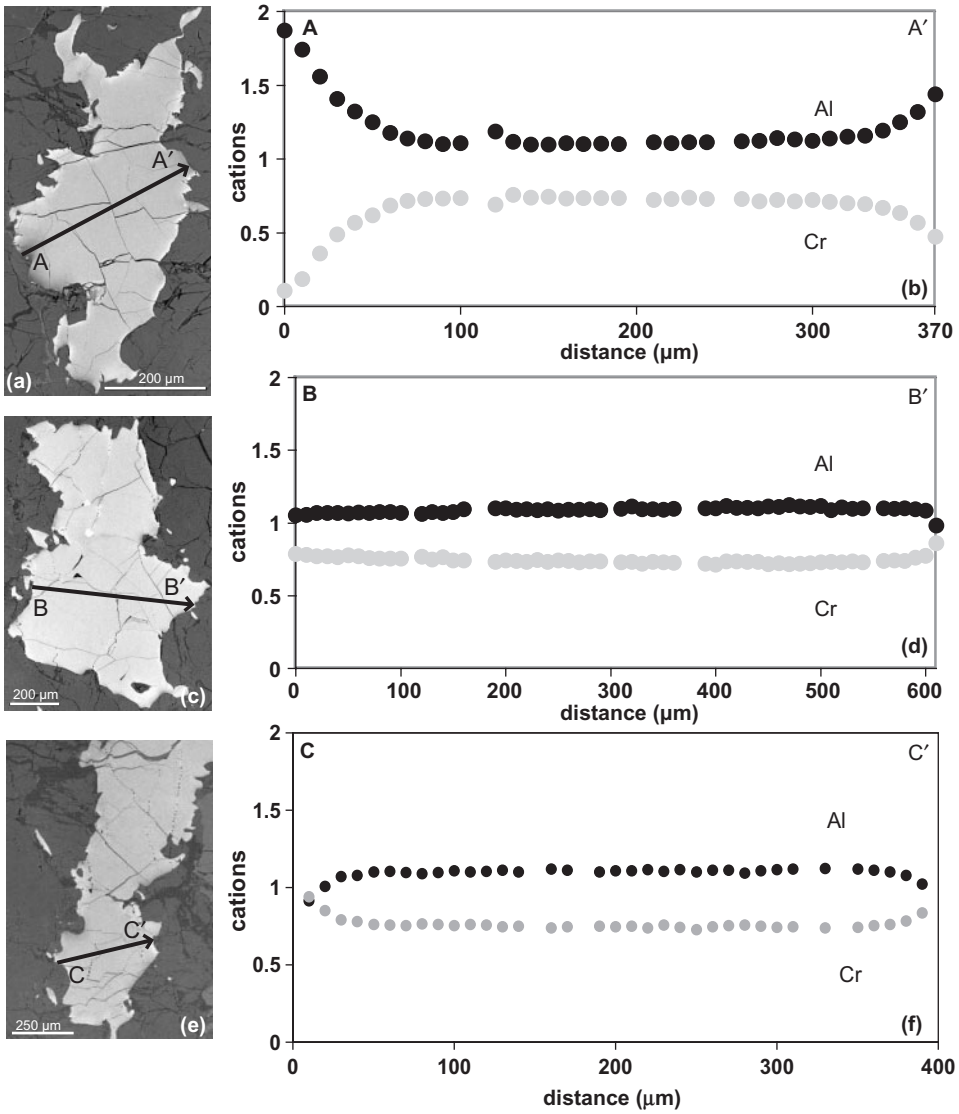

Fig. 13. Compositional cross-sections of spinel grains from the PFG and the proto-mylonite domain. (a, b) Zoning profile of a spinel grain surrounded by olivine (left) and orthopyroxene resulting in a Cr-number variation between 0·10 and 0·40. The spinel shows a distinct asymmetric zoning pattern inconsistent with overall equilibrium (La2002-5). (c, d) Zoning profile of spinel from a different microstructural domain, in the same sample (La2002-5). The grain is surrounded by plagioclase (left) and olivine (right). Al exhibits a weak decrease coupled with Cr increase (La2002-5). (e, f) Symmetric zoning of Al and Cr along the profile (L09). The grain is surrounded by plagioclase (left) and orthopyroxene (right).

related to melt–rock interaction and interstitial crystallization (e.g. Fig. 6).

Melt–rock reaction textures are more abundant in the central part than in the northern part of the Lanzo massif and in porphyroclastic textures than in the mylonite rocks, suggesting the following scenario to explain these observations: (1) melt impregnation preceded deformation then (2) the progressive mylonitization and recrystallization eliminated melt migration microstructures, and/or (3) melt impregnation was also contemporaneous with the major shearing event.

The presence of deformed microstructures in orthopyroxene and plagioclase replacing porphyroclastic clinopyroxene suggests that melt impregnation started before the onset of high-temperature shearing. The development of vermicular, interstitial orthopyroxene with its long axis parallel to the foliation (Fig. 5c), which is abundant in proto-mylonites and uncommon in the mylonites, also suggests that melt–rock reaction preceded and/or was contemporaneous with shearing, followed by integration of the interstitial orthopyroxene in the fine-grained matrix of the mylonite. Thus, the microtextural evidence indicates

Table 8: Thermometry of Lanzo peridotites based on coexisting pyroxenes and olivine–spinel equilibria

Thermometer:	$T_{2\text{-pyx}}$ BK90	$T_{\text{Ca-in-opx}}$ BK90	$T_{\text{Al,Cr opx}}$ WS91	$T_{\text{ol-sp}}$ Bal91	
Cores					
Mylonite with UMB	–	902 ± 7	1032 ± 7	944 ± 35	$n = 1$
Mylonite	–	954 ± 4	1101 ± 7	1136 ± 65	$n = 2$
Proto-mylonite	–	1017 ± 7	1063 ± 25	1051 ± 83	$n = 2$
PFG	–	970 ± 36	1069 ± 23	972 ± 20	$n = 2$
PC	–	960 ± 23	1030 ± 18	–	$n = 3$
PC-N	–	1003 ± 10	1070 ± 23	–	$n = 2$
Average		980 ± 28	1067 ± 23	1021 ± 93	
Rims					
Hydrous mylonite	770 ± 5	798 ± 6	826 ± 24	–	$n = 1$
Mylonite	862 ± 80	841 ± 1	779 ± 65	–	$n = 2$
Proto-mylonite	855 ± 19	903 ± 19	791 ± 37	–	$n = 2$
PFG	830 ± 19	909 ± 70	887 ± 46	–	$n = 2$
PC	809 ± 80	920 ± 43	901 ± 6	–	$n = 3$
PC-N	869 ± 90	917 ± 4	926 ± 31	–	$n = 2$
Average	839 ± 24	893 ± 36	840 ± 63	–	
Neoblasts					
Hydrous mylonite	800 ± 25	825 ± 11	–	598 ± 1	$n = 1$
Mylonite	890 ± 44	879 ± 12	–	774 ± 53	$n = 2$
Proto-mylonite	806 ± 42	891 ± 2	–	760 ± 74	$n = 2$
PFG	888 ± 84	912 ± 69	–	794 ± 18	$n = 2$
Average	861 ± 48	894 ± 17	–	776 ± 17	
Melt reaction cpx + liq → opx + plg (domain I)					
		950 ± 36	1053 ± 30		$n = 3$
Reaction ol + liq1 → opx + liq2 (domain II)					
Cores	–	951 ± 62	889 ± 61		$n = 10$
Rims	–	908 ± 28	821 ± 49		$n = 5$

The averages are calculated without the amph-rich mylonite. The temperature for each category is an average for 3–6 neighbouring grains and a minimum of two samples (n), except for the amph-rich mylonite ($n = 1$). opx, orthopyroxene; cpx, clinopyroxene; pyx, pyroxene; ol, olivine; sp, spinel; plg, plagioclase; liq, liquid. PFG: porphyroclastic fine-grained; PC: porphyroclastic; PC-N porphyroclastic-north. BK90, Brey & Kohler (1990); WS91, Witt-Eickschen & Seck (1991); Bal91, Ballhaus *et al*. (1991).

that reactive porous flow of melt precedes high-temperature deformation. The preferential orientation of plagioclase-bearing aggregates along the spinel foliation planes (Fig. 3) may indicate deformation-enhanced melt migration. This microtexture indicates an incongruent reaction

$$\text{Al-rich spinel} + \text{Liq } 1 \rightarrow \text{Cr-spinel} + \text{plagioclase} + \text{Liq } 2. \quad (3)$$

Plagioclase is not always associated with spinel, but also forms aggregates parallel to the foliation associated with olivine, orthopyroxene, and clinopyroxene. The reactive fractionation process added basaltic components by interstitial crystallization of pyroxenes and plagioclase, which reduced the permeability of the peridotite. The chemical composition of the peridotite indicates a large range of composition from fertile plagioclase peridotite to refractory harzburgite and dunite (Bodinier, 1988; Kaczmarek & Müntener, submitted). Deformed peridotites tend to be compositionally more homogeneous and fertile than weakly porphyroclastic peridotite. The peridotite from the mylonite area displays major element (e.g. Al, Na) and rare earth element (e.g. La, Yb) enrichment. The high modal abundance of plagioclase, coupled with bulk chemical compositions partially exceeding primitive upper mantle values, suggests that the top of the shear zone acts as a melt focusing zone, with volumetrically abundant accumulation of melt.

However, microstructural evidence in the peridotite mylonites clearly shows that deformation occurred in the

presence of melt and outlasted interstitial melt crystallization. Deformation and melt migration are complex processes that interact with each other (e.g. Kohlstedt & Zimmerman, 1996; Kelemen *et al.*, 1997*a*; Holtzman *et al.*, 2003). The-fine grained areas (5–50 mm) are probably produced during subsolidus deformation, but the grain size may have been larger during melt migration. Thus, the shear zones would have had a relatively high permeability at that stage (see also Holtzman & Kohlstedt, 2007). In addition, the presence of melt during deformation has a pronounced effect on the distribution of strain and on grain-size reduction (Rosenberg & Handy, 2001). Strain is more homogeneously distributed in melt-free samples (Rosenberg & Handy, 2000). Rosenberg & Handy (2000, 2001) experimentally demonstrated strain localization within melt-bearing, extensional shear fractures. In the same way, Holtzman *et al.* (2003) and Holtzman & Kohlstedt (2007) demonstrated that in partially molten rocks deformed at high temperature and pressure, melt segregates spontaneously and organizes into a melt-rich network in which permeability is higher than in the surrounding peridotites (Fig. 14). In summary, we propose that shearing associated with melt percolation in the Lanzo shear zones implies both localization of the deformation and focusing of melt transport.

Once the shear zone cooled below the solidus the melt-rich bands crystallized to a fine-grained assemblage. It is interesting to speculate that the field relationships and the spatial distribution of MORB-type gabbroic dykes are related to the location of peridotite mylonites. In the footwall of the shear zone, hydrofracturing and the MOR-type gabbroic dykes are clearly discordant to the high-temperature foliation, whereas in the peridotite mylonites the gabbroic dykes are parallel to the foliation. Thus, hydrostatic overpressure that formed the gabbroic dykes is probably not sufficient to overcome the strength of the actively deforming peridotite mylonites. Our field observations on the spatial distribution of gabbroic dykes (Fig. 2), which are preferentially observed in the footwall of the peridotite mylonite zone, support this hypothesis.

Fabric variation across the shear zone

The inhomogeneous distribution of porphyroclastic lithologies across the mylonite zone and the variation of grain sizes over approximately three orders of magnitude indicate that different deformation mechanisms operated

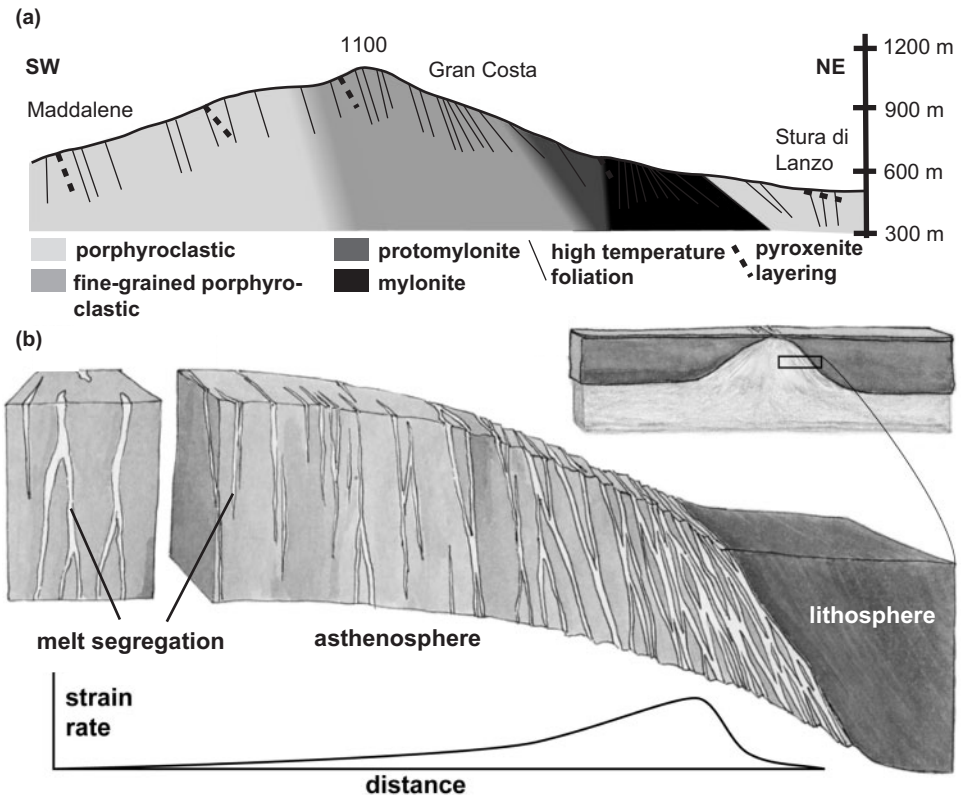

Fig. 14. (a) Simplified profile across the Lanzo shear zone, with a gradient in deformation structures from the shear zone to the porphyroclastic peridotites. (b) A schematic illustration of the spatial distribution of structures formed by stress-driven melt segregation (from Holtzman & Kohlstedt, 2007). It should be noted that the Lanzo example illustrates a finite stage, combining supersolidus and subsolidus deformation, whereas the illustration of Holtzman & Kohlstedt illustrates the stage of active stress-driven melt segregation.

during the development of the Lanzo shear zone. The presence of large, sometimes equant porphyroclasts indicates that the rheology of the peridotite shear zone is grain-size sensitive and that localization of deformation is an important process. The progressive mylonitization is marked by increasing volume fractions of very fine-grained matrix domains that form up to 80% of the mylonite. Deformation probably occurred in a grain-size sensitive creep regime, as suggested by the fine-grained matrix (<10 μm). The fine-grained, proto-mylonite and mylonite rocks have asymmetric bands of recrystallized grains, indicating dominantly non-coaxial deformation of the peridotites. An important observation is that grain-size variation is correlated with the presence or absence of secondary phases. Aggregates of 'pure' olivine show grain sizes an order of magnitude larger than polyphase recrystallized bands. Similar observations have also been made on samples from oceanic fracture zones (Warren & Hirth, 2006). The type of minerals that compose the polyphase bands influences the weakening of the system. Olivine is considered to be a weak mineral, which largely controls the deformation fabric in the mantle. In addition, the presence of plagioclase may influence the localization of deformation. Newman *et al.* (1999) identified the subsolidus plagioclase-forming reaction as a major mechanism for grain-size reduction in a Pyrenean peridotite shear zone. Vissers *et al.* (1991, 1995) interpreted polyphase, fine-grained mantle shear zones in the Erro–Tobbio peridotites as resulting from hydration reactions and related grain-size reduction. An alternative mechanism was proposed for the Othris peridotite (Greece), where grain-size reduction was suggested in part to be induced by melt-present reactions (Dijkstra *et al.*, 2002). As outlined above, plagioclase is present everywhere in the Lanzo peridotite, and its modal abundance is not restricted to peridotite mylonites, The presence of plagioclase as a weak mineral will strongly determine the localization of the deformation (Newman *et al.*, 1999). In the mylonite samples, the plagioclase is evenly distributed and sometimes forms a network in the fine-grained bands; elsewhere, it is sometimes preserved as lenses in the less deformed areas. Taken together, the presence of various igneous reaction textures, the localization of the deformation and the grain-size reduction all indicate that melt-enhanced deformation played a major role in the evolution of the Lanzo shear zone.

The occurrence of interstitial orthopyroxene associated with olivine (domain II, ol + opx) in the mylonite and the fine-grained bands suggests that there are two processes that control the evolution of grain size during continuing deformation: (1) the chemistry of migrating basaltic liquids in the deformed peridotites; (2) the continuing cooling to lower temperatures during deformation. Disequilibrium textures between mantle minerals suggest that the chemistry of the ephemeral migrating liquid is locally controlled. Thus, the peridotite–melt system may not be multiply saturated everywhere, and orthopyroxene–olivine reaction relationships predominate. This microstructure is present in pressure shadows of polycrystalline olivine bands and porphyroclasts, suggesting that melt migration began before the intense deformation event. The olivine–orthopyroxene equilibrium is extremely sensitive to small chemical, thermal or pressure variations, as shown by experimental investigations (Villiger *et al.*, 2004), and it is thus not surprising that olivine-producing and olivine-consuming microstructures have been observed in the same area (Dijkstra *et al.*, 2002). Experimental deformation of peridotite also shows 'equilibrated' and 'non-equilibrated' microstructures between olivine and melt (e.g. Holtzman *et al.*, 2003). Because olivine and orthopyroxene are in a peritectic reaction relationship, pinning might be less effective because orthopyroxene grows at the expense of olivine, a feature reflected by grain sizes that are significantly larger than in polyphase mylonitic bands.

To evaluate the conditions in which the polyphase melt-rich bands formed, we recall that the chemical composition of migrating basaltic liquid is generally buffered by the peridotite matrix. Multiple saturation will lead to efficient crystallization of the interstitial liquid, forming microgabbroic assemblages; however, substantial grain growth is inhibited by the simultaneous crystallization of olivine, plagioclase and pyroxenes. As deformation continues to lower temperatures and higher stresses (Vissers *et al.*, 1995), the initial mix of small grain sizes results in the pinning of grain boundaries, eventually leading to diffusion creep. Thus, we propose that a combination of melt-enhanced deformation at an early stage followed by recrystallization coupled to the pinning effects of secondary phases (Olgaard & Evans, 1988; Herwegh *et al.*, 2005) can explain the inhomogeneous fine-grained shear zones in the Lanzo peridotite.

Disequilibrium mineral compositions and relationship to microstructures

The chemical variation of orthopyroxene and clinopyroxene from core to rim (decrease in Al and Cr) is a marker of retrogression (decreasing P–T) from spinel peridotite to plagioclase peridotite facies and is observed in all rock types. These observations were recently confirmed by an experimental study (Borghini *et al.*, 2007). Relics of a precursor equilibration in the spinel peridotite field are preserved by rare opx and cpx porphyroclast cores. However, the systematic chemical variation of orthopyroxene with respect to its microstructure indicates that overall chemical equilibrium on a thin-section scale has not been achieved (see below). The thermometric calculations indicate a cooling history that started at high temperatures in the spinel lherzolite field (Pognante *et al.*, 1985), finally ending in the plagioclase lherzolite field.

The widespread occurrence of Ti-hornblende in the recrystallized matrix of the peridotites indicates the presence of a fluid or silicate melt during deformation, at temperatures not exceeding 1050°C for the final crystallization of hornblende (Niida & Green, 1999).

The spinel chemistry shows large compositional variations observed on the grain to intra-sample scale. The chemical variation covers almost the entire field of spinel from abyssal spinel peridotites (Dick & Bullen, 1984), and indicates disequilibrium in the plagioclase facies (Cr- and Ti-rich spinel). The Cr-number of spinel has been shown to be a sensitive indicator for melt extraction (Dick & Bullen, 1984; Dick *et al.*, 1984; Michael & Bonatti, 1985; Dick, 1989), melt peridotite reaction during focused porous flow (Kelemen *et al.*, 1992; Allan & Dick, 1996; Dick & Natland, 1996; Kelemen *et al.*, 1997*b*) and melt–wallrock reactions in the vicinity of intruding magmatic veins (Cannat *et al.*, 1997*b*; Hellebrand *et al.*, 1999). With increasing degree of melting, the decreasing activity of Al in the peridotite leads to an increase of the equilibrium Cr-number in spinel. However, spinel formed by reaction with a migrating silicate liquid records enrichment in Cr and a concomitant decrease in Al [by reaction (3)], as shown in Fig. 13. The chemical zoning in single grains may also be induced by melt interaction or, alternatively, by stress (Ozawa, 1989). Stress chemical zoning leads to Al enrichment at the rim parallel to the lineation. This effect cannot entirely be excluded in the Lanzo massif, but was not observed in our samples. Indeed, Al enrichment is not symmetrical on each side of the grains we studied, but is irregular, and when symmetrical zoning is seen it is perpendicular rather than parallel to the lineation (see Fig. 13). Our preferred scenario is therefore that the irregular zoning results from interaction with migrating silicate melts. The TiO_2 enrichment in spinel coexisting with plagioclase cannot be explained by simple fractional crystallization in a closed system (e.g. Villiger *et al.*, 2004), but must be related to reactive fractionation of migrating silicate liquid within a peridotite matrix. The Ti content in many of our samples exceeds that obtained by experimental subsolidus reactions (G. Borghini, personal communication).

The most variable composition of spinel is found in the porphyroclastic samples; its high TiO_2 content strongly suggests *in situ* crystallization of ephemeral, small melt fractions, producing (micro-)gabbroic assemblages. A characteristic feature is that the extreme variability is recorded only by mineral compositions and not by whole-rocks (Kaczmarek & Müntener, 2009), which supports the hypothesis of nearly complete solidification without major escape of residual liquid out of the peridotite. The crystallization of melt by reaction in the shallow mantle explains why some parameters show little compositional variation (e.g. Mg-number), whereas others show extreme enrichment (e.g. TiO_2 in spinel). This process could potentially take place at near-isothermal conditions, although the widespread interstitial crystallization of Ti-hornblende suggests a final crystallization temperature of less than 1050°C. Small amounts of H_2O are not uncommon in MORB-type liquids (e.g. Michael & Chase, 1987), and H_2O enrichment during fractional crystallization will ultimately saturate ephemeral liquids in hornblende, as shown for ophiolitic and oceanic gabbros (e.g. Dick *et al.*, 2000; Tribuzio *et al.*, 2000; Desmurs *et al.*, 2002).

The porphyroclastic samples from the northern part of the Lanzo massif contain spinel of more homogeneous composition (compared with those from the central part) in equilibrium with plagioclase (Table 5). This remarkable difference between the porphyroclastic south and porphyroclastic north probably indicates a relatively different exhumation history for the two peridotite bodies: we propose that the central body records more rapid exhumation from spinel facies to plagioclase facies with respect to the northern part.

It is interesting to speculate about the effects of homogenization of spinel compositions by progressive localization of deformation and concomitant grain-size reduction and simple cooling. It is possible that decreasing temperatures under subsolidus conditions coupled with grain-size reduction erased and/or homogenized most of the disequilibrium spinel compositions. However, an alternative is that melt migration along actively deforming shear zones precludes extreme fractionation of basaltic liquids, and thus extremely TiO_2-rich spinel compositions never developed.

Thermal constraints on the mantle shear zone

To understand the significance of the temperature discrepancy between porphyroclasts and neoblasts and the discrepancy between the thermometers (Table 8), it is important to briefly address the approximate relative equilibration velocity of various thermometers. Solid-state volume Fe–Mg exchange between olivine and spinel is considered to be a fast process (Ballhaus *et al.*, 1991) compared with Ca–Mg or Al diffusion in pyroxene. If we consider slow cooling, calculated temperatures will be controlled by the diffusion velocity of different chemical species, and thus will be lowest for Fe–Mg exchange between olivine and spinel and highest for Al in orthopyroxene.

Calculations using core compositions and using fast and slowly reacting thermometers ($T_{\mathrm{Al,Cr\text{-}in\text{-}opx\ WS91}}$, $T_{\mathrm{Fe–Mg,\ ol–spl\ B91}}$) result in similar temperatures, suggesting that cooling of the mylonites was fast enough to not significantly affect core compositions by solid-state diffusion. If we consider the results from the neoblasts (Table 8), Ca-in-opx provides temperatures that are ~100°C higher than olivine–spinel thermometry, suggesting that cooling was slow enough to affect small neoblasts but not large

porphyroclasts. We thus conclude that chemical equilibration among different recrystallized minerals within the mylonites is controlled by dynamic recrystallization, and not by solid-state diffusion. Therefore rapid exhumation is required to retain high temperatures in the porphyroclasts, in particular for olivine–spinel pairs.

Geodynamic implications

The Lanzo shear zone is an exceptional area to study the relationships between reactive fractionation of migrating silicate liquids and deformation. However, the Lanzo massif also records subduction up the eclogite facies during the Alpine collision (Pelletier & Müntener, 2006). The subduction probably induced important rigid body rotations. Because of its allochthonous nature the original orientation of the shear zone and associated relative movements prior to the Alpine collisonal history are difficult to restore, and the absolute movement between the central and the northern body of the Lanzo peridotite cannot be quantified. However, the distribution of mafic dykes, combined with the overall structure and geochemistry of the Lanzo peridotite, allows us to propose a schematic tectonic model. The southern body has been interpreted as asthenospheric mantle (Bodinier, 1988; Bodinier *et al.*, 1991) whereas the northern body exhibits lithospheric affinities, suggesting an original polarity.

Previous geochemical studies on the Lanzo massif demonstrate a fertile composition with respect to primitive mantle abundances and the presence of numerous mafic rocks (Boudier & Nicolas, 1972; Boudier, 1978; Bodinier, 1988). More recent studies have demonstrated that the peridotite was refertilized by near-solidus reactive fractionation of migrating basaltic liquid on a kilometre scale (e.g. Müntener & Piccardo, 2003; Müntener *et al.*, 2005), followed by progressive localization of melt flow. Here we infer that actively deforming shear zones may focus migrating liquid at an early stage, and later, under subsolidus conditions, they act as a permeability barrier to dyke propagation across the shear zone. Figure 15 illustrates

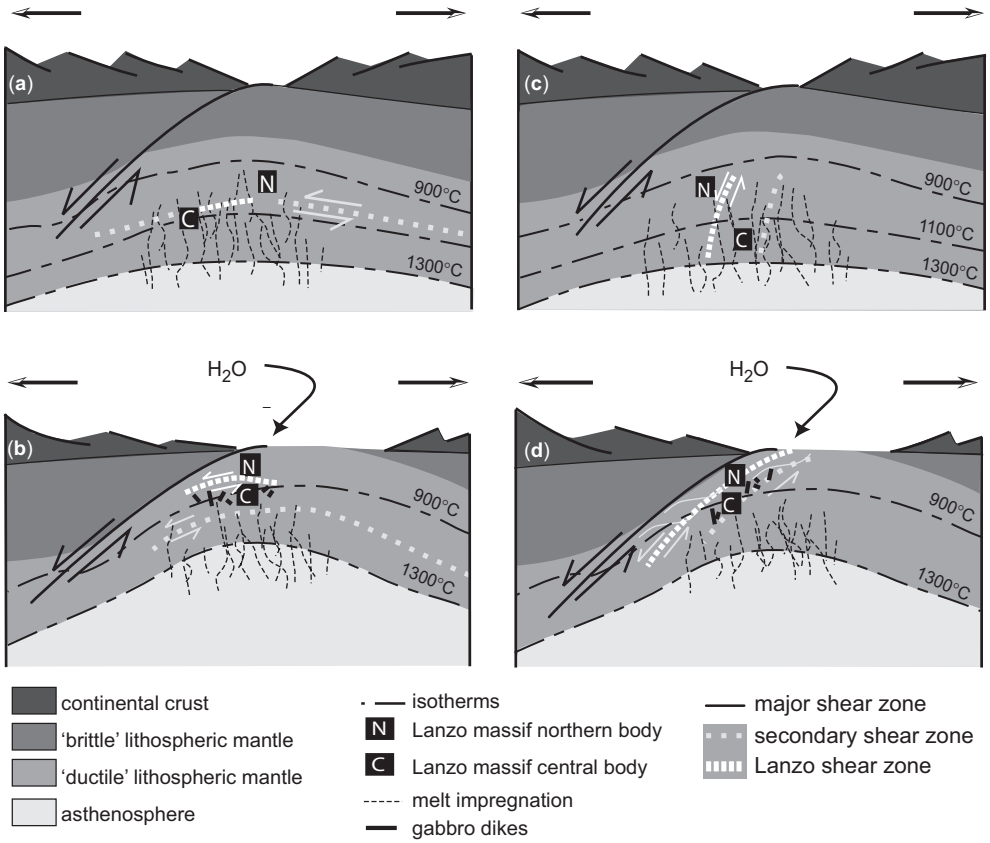

Fig. 15. Conceptual model for the evolution of the high-temperature mantle shear zone of the Lanzo peridotite during the advanced stages of rifting. Sketches illustrate the approximate position of the Lanzo massif in the lithosphere during mantle exhumation before break-up. (a, b) and (c, d) represent two alternative views of the early stage of the exhumation supported by existing models: Lavier & Manatschal (2006), and Lemoine *et al.* (1987), respectively. Initial extension of the lithosphere generates shear zones including the Lanzo shear zone parallel to the base of the lithosphere (a) or parallel to a pre-existing extensional shear zone (c). Both the northern (N) and the central (C) body are initially in the spinel peridotite facies and are later impregnated by melt. (b) and (d) represent rapid exhumation of mantle peridotite, decreasing temperature, hydration of the top of the shear zone by infiltrating fluids, and formation of MORB-type gabbro dykes cross-cutting the high-temperature foliation (Kaczmarek *et al.*, 2008). Arrows indicate the extension direction.

two possible scenarios with which to interpret our observations in the context of mantle exhumation and establishment of an ocean–continent transition zone or an (ultra-)slow-spreading ridge. Either (1) the initiation of the shear zone was subparallel to the lithosphere, as suggested by recent numerical modelling of Lavier & Manatschal (2006), or (2) the shear zone was part of a major low-angle extensional system (e.g. Lemoine *et al.*, 1987; Lagabrielle & Lemoine, 1997). The early stage (Fig. 15a and c) represents the northern and central body at depth close to the 1100°C isotherm. Continuing extension progressively exhumes the mantle shear zones (Fig. 15b and d), and eventually such shear zones are finally exposed on the ocean floor (presence of mylonite with ultra-mylonite bands at the top of the central body; Fig. 2). Thermometry on neoblasts indicates cooling to 860°C or 800°C in the mylonite with ultra-mylonite bands. This temperature decrease is unrelated to the exhumation of the massif from spinel to plagioclase facies. In both scenarios, actively deforming shear zones would accumulate igneous material (dykes and sills) in the footwall, which might be separated from early serpentinization at shallower levels in the hanging wall. Alternatively, the early stage of the shear zone(s) was much steeper (Fig. 15b and c) and conceptually similar to the original proposal of Nicolas *et al.* (1972). This alternative scenario allows for a more rapid exhumation of mantle rocks, consistent with evidence from spinel disequilibrium conditions and particularly between the central and the northern bodies.

CONCLUSIONS

The petrological and microstructural investigations of a kilometre-scale mantle shear zone in the Lanzo peridotite demonstrate that high-temperature deformation is progressively localized towards fine-grained mylonites that were active in the plagioclase peridotite facies. Microchemical analyses of spinel and pyroxenes suggest that significant disequilibrium compositions are preserved, which cannot simply be explained by cooling during exhumation. Instead, large chemical variations are produced by ephemeral melts that crystallize in the Lanzo peridotite. Our microstructural observations suggest that grain-size reduction by incongruent melt–rock reactions coupled with active deformation provide a mechanism for initial weakening and strain localization at temperatures exceeding 1000°C. Grain boundary pinning in areas of incongruent melt–rock reactions may counterbalance the tendency of rapid grain growth in the presence of basaltic melts. During exhumation and cooling, further reduction in grain size combined with second phase pinning provide a mechanism to maintain shear localization over a large temperature interval, probably down to 600°C.

Our field observations on the distribution of mafic dykes are consistent with an interpretation that actively deforming mantle shear zones at subsolidus conditions may act as permeability and thermal barriers for the upward migration of hydrofractures. Thus migrating mafic magma may be forced to stall beneath such permeability barriers and form gabbro sills, providing a mechanism to explain high-pressure gabbro crystallization in the oceanic lithosphere along (ultra-)slow-spreading ridges.

ACKNOWLEDGEMENTS

We thank Arjan Dijkstra, Marco Herwegh, Uli Faul, Gianreto Manatschal, Luc Lavier and Giovanni Piccardo for many controversial and fruitful discussions. Detailed reviews by E. Hellebrand, G. Suhr and B. Holtzman, and editorial comments by C. Devey substantially improved the manuscript and are gratefully acknowledged. This research was financially supported by the Swiss National Science Foundation (Grants 21-66923.01 and 200020-104636/1).

SUPPLEMENTARY DATA

Supplementary data for this paper are available at *Journal of Petrology* online.

REFERENCES

Allan, J. F. & Dick, H. J. B. (1996). Cr-rich spinel as a tracer for melt migration and melt-wall rock interaction in the mantle: Hess Deep, Leg 147. In: Gillis, M. C., Allan, K. M. & Meyer, P. S. (eds) *Proceedings of the Ocean Drilling Program, Scientific Results, 147.* College Station, TX: Ocean Drilling Program, pp. 157–172..

Ballhaus, C., Berry, R. F. & Green, D. H. (1991). High pressure experimental calibration of the olivine–orthopyroxene–spinel oxygen geobarometer; implications for the oxidation state of the upper mantle. *Contributions to Mineralogy and Petrology* **107**, 27–40.

Bente, K. & Lensch, G. (1981). Studies of retromorphosed dikes of southern Lanzo peridotite massif, Italian Western Alps. *Schweizerische Mineralogische und Petrographische Mitteilungen* **61**, 297–303.

Bodinier, J.-L. (1988). Geochemistry and petrogenesis of the Lanzo peridotite body, Western Alps. *Tectonophysics* **149**, 67–88.

Bodinier, J.-L., Guirard, M., Dupuy, C. & Dostal, J. (1986). Geochemistry of basic dikes in the Lanzo massif (Western Alps): petrogenetic and geodynamic implications. *Tectonophysics* **128**, 77–95.

Bodinier, J.-L., Menzies, M. A. & Thirlwall, M. F. (1991). Continental to oceanic mantle transition—REE and Sr–Nd isotopic geochemistry of the Lanzo lherzolite massif. *Journal of Petrology Special Lherzolite Issue*, 191–210.

Borghini, G., Fumagalli, P. & Rampone, E. (2007). Experimental and natural constraints on the spinel–plagioclase subsolidus transition in mantle peridotite. In: *European Geosciences Union.* Vienna: Geophysical Research.

Boudier, F. (1972). Relations lherzolites–gabbro–dunite dans le massif de Lanzo (Alpes Piémontaises): exemple de fusion partielle. Université de Nantes.

Boudier, F. (1978). Structure and petrology of the Lanzo peridotite massif (Piedmont Alps). *Geological Society of America Bulletin* **89**, 1574–1591.

Boudier, F. & Nicolas, A. (1972). Fusion partielle gabbroique dans la lherzolite de Lanzo (Alpes Piémontaises). *Bulletin Suisse de Minéralogie et de Pétrographie* **52**, 39–56.

Brey, G. P. & Köhler, T. (1990). Geothermobarometry in four-phase lherzolites II. New thermobarometers, and practical assessment of existing thermobarometers. *Journal of Petrology* **31**, 1353–1378.

Cannat, M. (1993). Emplacement of mantle rocks in the seafloor at mid-ocean ridges. *Journal of Geophysical Research* **98**, 4163–4172.

Cannat, M., Chatin, F., Whitechurch, H. & Ceuleneer, G. (1997*a*). Gabbroic rocks trapped in the upper mantle at the mid-atlantic ridge. In: Karson, J. A., Cannat, M., Miller, D. J. & Elton, D. (eds) *Proceedings of the Ocean Drilling Program, Scientific Results, 153*. College Station, TX: Ocean Drilling Program, pp. 243–264.

Cannat, M., Lagabrielle, Y., Bougault, H., Casey, J., de Coutures, N., Dmitriev, L. & Fouquet, Y. (1997*b*). Ultramafic and gabbroic exposures at the Mid-Atlantic Ridge: geological mapping in the 15°N region. *Tectonophysics* **279**, 193–213.

Desmurs, L., Müntener, O. & Manatschal, G. (2002). Onset of magmatic accretion within a magma-poor rifted margin: a case study from the Platta ocean–continent transition, eastern Switzerland. *Contributions to Mineralogy and Petrology* **144**, 365–382.

Dick, H. J. B. (1989). Abyssal peridotites, very slow spreading ridges and ocean ridge magmatism. In: Saunders, A. D. & Norry, M. J. (eds) *Magmatism in the Ocean Basins. Geological Society, London, Special Publications* **42**, 71–105.

Dick, H. J. B. & Bullen, T. (1984). Chromian spinel as a petrogenetic indicator in abyssal and alpine-type peridotites and spatially associated lavas. *Contributions to Mineralogy and Petrology* **86**, 54–64.

Dick, H. J. B. & Natland, J. H.. (1996). Late-stage melt evolution and transport in the shallow mantle beneath the East Pacific Rise. In: Gillis, M. C., Allan, K. M. & Meyer, P. S. (eds) *Proceedings of the Ocean Drilling Program, Scientific Results, 147*. College Station, TX: Ocean Drilling Program, pp. 103–134.

Dick, H. J. B., Fisher, R. L. & Bryan, W. B. (1984). Mineralogic variability of the uppermost mantle along mid-ocean ridges. *Earth and Planetary Science Letters* **69**, 88–106.

Dick, H. J. B., Natland, J. H., Alt, J. C. *et al*. (2000). A long *in situ* section of the lower ocean crust: results of ODP Leg 176 drilling at the Southwest Indian Ridge. *Earth and Planetary Science Letters* **179**, 31–51.

Dijkstra, H. A., Drury, M. R., Vissers, R. L. M. & Newman, J. (2002). On the role of melt–rock reaction in mantle shear zone formation in the Othris peridotite massif (Greece). *Journal of Structural Geology* **24**, 1431–1450.

Drury, M. R. (2005). Dynamic recrystallization and strain softening of olivine aggregates in the laboratory and the lithosphere. In: Gapais, D., Brun, J. P. & Cobbold, P. R. (eds) *Deformation Mechanisms, Rheology and Tectonics: from Minerals to the Lithosphere. Geological Society, London, Special Publications* **243**, 143–158.

Drury, M. R. & Fitz Gerald, J. D. (1998). Mantle rheology: insights from laboratory studies of deformation and phases transition. In: Jackson, I. (ed.) *The Earth's Mantle: Composition, Structure, and Evolution*. Cambridge: Cambridge University Pres, pp. 503–559.

Drury, M. R., Hoogerduijn Strating, E. H. & Vissers, R. L. M. (1990). Shear zone structures and microstructures in mantle peridotites from the Voltri Massif, Ligurian Alps, N. W. Italy. *Geologie en Mijnbouw* **69**, 3–17.

Ernst, W. G. & Piccardo, G. B. (1979). Petrogenesis of some Ligurian Peridotites; I Mineral and bulk-rock chemistry. *Geochimica et Cosmochimica Acta* **43**, 219–238.

Gasparik, T. (1987). Orthopyroxene thermometry in simple and complex systems. *Contributions to Mineralogy and Petrology* **96**, 357–370.

Hellebrand, E. & Snow, J. E. (2003). Deep melting and sodic metasomatism underneath the highly oblique-spreading Lena Trough (Arctic Ocean). *Earth and Planetary Science Letters* **216**, 283–299.

Hellebrand, E., Snow, J. E., Dick, H. J. B., Devey, C. W. & Hofmann, A. W. (1999). Reactive crack flow in the oceanic mantle: an ion probe study on cpx from vein-bearing abyssal peridotites. *Ofioliti* **24**, 106–107.

Hellebrand, E., Snow, J., Dick, H. J. B. & Hofmann, A. W. (2001). Coupled major and trace elements as indicators of the extent of melting in mid-ocean-ridge peridotites. *Nature* **410**, 677–681.

Hellebrand, E., Snow, J., Mostefaoui, S. & Hoppe, P. (2005). Trace element distribution between orthopyroxene and clinopyroxene in periodotites from the Gakkel Ridge; a SIMS and NanoSIMS study. *Contributions to Mineralogy and Petrology* **150**, 486–504.

Herwegh, M., Berger, A. & Ebert, A. (2005). Grain coarsening maps: a new tool to predict microfabric evolution of polymineralic rocks. *Geology* **33**, 801–804.

Hirth, G. & Kohlstedt, D. L. (1995). Experimental constraints on the dynamics of the partially molten upper mantle; deformation in the diffusion creep regime. *Journal of Geophysical Research* **100**, 1981–2001.

Holtzman, B. K. & Kohlstedt, D. L. (2007). Stress-driven melt segregation and strain partitioning in partially molten rocks: Effects of stress and strain. *Journal of Petrology* **48**, 2379–2406.

Holtzman, B. K., Kohlstedt, D. L., Zimmerman, M. E., Heidelbach, F., Hiraga, T. & Hustoft, J. (2003). Melt segregation and strain partitioning: implications for seismic anisotropy and mantle flow. *Science* **301**, 1227–1230.

Jaroslow, G. E., Hirth, G. & Dick, H. J. B. (1996). Abyssal peridotite mylonites: implications for grain-size sensitive flow and strain localization in the oceanic lithosphere. *Tectonophysics* **256**, 17–37.

Kaczmarek, M.-A. & Müntener, O. (2009). The influence of melt impregnation and high temperature shear zones on peridotite geochemistry (Lanzo massif, Italy). *Earth and Planetary Science Letters* (submitted).

Kaczmarek, M.-A., Müntener, O. & Rubatto, D. (2008). Trace element chemistry and U–Pb dating of zircons from oceanic gabbros and their relationship with whole rock composition (Lanzo, Italian Alps). *Contributions to Mineralogy and Petrology* **155**, 295–312.

Kelemen, P. B., Dick, H. J. B. & Quick, J. E. (1992). Formation of harzburgite by pervasive melt/rock reaction in the upper mantle. *Nature* **358**, 635–641.

Kelemen, P. B., Hirth, G., Shimizu, N., Spiegelman, M. & Dick, H. J. B. (1997*a*). A review of melt migration processes in the adiabatically upwelling mantle beneath oceanic spreading ridges. *Philosophical Transactions of the Royal Society of London* **355**, 283–318.

Kelemen, P. B., Koga, K. & Shimizu, N. (1997*b*). Geochemistry of gabbro sills in the crust–mantle transition zone of the Oman ophiolite: implications for the origin of the oceanic lower crust. *Earth and Planetary Science* **146**, 475–488.

Kienast, J. R. & Pognante, U. (1988). Chloritoid-bearing assemblages in eclogitized metagabbros of the Lanzo peridotite body (western Italian Alps). *Lithos* **21**, 1–11.

Klemme, S. & O'Neill, H. S. C. (2000). The near-solidus transition from garnet lherzolite to spinel lherzolite. *Contributions to Mineralogy and Petrology* **138**, 237–248.

Kohlstedt, D. L. & Zimmerman, M. E. (1996). Rheology of partially molten mantle rocks. *Annual Review of Earth and Planetary Sciences* **24**, 41–62.

Lagabrielle, Y. & Lemoine, M. (1997). Alpine, Corsican and Apennine ophiolites: the slow-spreading ridge model. *Comptes Rendus de l'Académie des Sciences* **325**, 909–920.

Lavier, L. L. & Manatschal, G. (2006). A mechanism to thin the continental lithosphere at magma-poor margins. *Nature* **440**, 324–328.

Lemoine, M., Tricart, P. & Boillot, G. (1987). Ultramafic and gabbroic ocean floor of the Ligurian Tethys (Alps, Corsica, Apennines): In search of a genetic model. *Geology* **15**, 622–625.

Mercier, J.-C. C. & Nicolas, A. (1975). Textures and fabrics of upper-mantle peridotites as illustrated by xenoliths from basalts. *Journal of Petrology* **16**, 454–487.

Michael, P. J. & Bonatti, E. (1985). Peridotite composition from the North Atlantic; regional and tectonic variations and implications for partial melting. *Earth and Planetary Science Letters* **73**, 91–104.

Michael, P. J. & Chase, R. L. (1987). The influence of primary magma composition, H_2O and pressure on midocean ridge basalt differentiation. *Contributions to Mineralogy and Petrology* **96**, 245–263.

Müntener, O. & Piccardo, G. B. (2003). Melt migration in ophiolitic peridotites: the message from Alpine–Apennine peridotites and implications for embryonic ocean basins. In: Dilek, Y. & Robinson, P. T. (eds) *Ophiolites in Earth History. Geological Society, London, Special Publications* **218**, 69–89.

Müntener, O., Hermann, J. & Trommsdorff, V. (2000). Cooling history and exhumation of lower-crustal granulite and upper mantle (Malenco, Eastern Central Alps). *Journal of Petrology* **41**, 175–200.

Müntener, O., Pettke, T., Desmurs, L., Meier, M. & Schaltegger, U. (2004). Refertilization of mantle peridotite in embryonic ocean basins: trace element and Nd isotopic evidence and implications for crust–mantle relationships. *Earth and Planetary Science Letters* **221**, 293–308.

Müntener, O., Piccardo, G. B., Polino, R. & Zanetti, A. (2005). Revisiting the Lanzo peridotite (NW-Italy): "asthenospherization" of ancient mantle lithosphere. *Ofioliti* **30**, 111–124.

Newman, J., Lamb, W. M., Drury, M. R. & Vissers, R. L. M. (1999). Deformation processes in a peridotite shear zone: reaction-softening by an H_2O-deficient, continuous net transfert reaction. *Tectonophysics* **303**, 193–222.

Nicolas, A. (1986). A melt extraction model based on structural studies in mantle peridotites. *Journal of Petrology* **27**, 999–1022.

Nicolas, A., Bouchez, J.-L. & Boudier, F. (1972). Kinematic interpretation of plastic deformations in the lherzolite Massif of Lanzo (Piedmont Alps); comparison with other massifs. *Tectonophysics* **14**, 143–171.

Niida, K. & Green, D. H. (1999). Stability and chemical composition of pargasitic amphibole in MORB pyrolite under upper mantle conditions. *Contributions to Mineralogy and Petrology* **135**, 18–40.

Olgaard, D. L. & Evans, B. (1988). Grain growth in synthetic marbles with added mica and water. *Contributions to Mineralogy and Petrology* **100**, 246–260.

Ozawa, K. (1989). Stress induced Al/Cr zoning of spinel in deformed peridotite. *Nature* **338**, 141–144.

Ozawa, K. & Takahashi, N. (1995). *P–T* history of mantle diapir: the Horoman peridotite complex, Hokkaido, northern Japan. *Contributions to Mineralogy and Petrology* **120**, 223–248.

Pelletier, L. & Müntener, O. (2006). High pressure metamorphism of the Lanzo peridotite and its oceanic cover, and some consequences for the Sesia–Lanzo zone (northwestern Italian Alps). *Lithos* **90**, 111–130.

Piccardo, G. B., Müntener, O., Zanetti, A. & Pettke, T. (2004). Ophiolitic peridotites of the Alpine Apennine system: mantle processes and geodynamic relevance. *International Geology Review* **46**, 1119–1159.

Piccardo, G. B., Zanetti, A. & Müntener, O. (2007). Melt/peridotite interaction in the Southern Lanzo peridotite: Field, textural and geochemical evidence. *Lithos* **94**, 181–209.

Pognante, U., Rösli, U. & Toscani, L. (1985). Petrology of ultramafic and mafic rocks from the Lanzo peridotite body (western Alps). *Lithos* **18**, 201–214.

Rosenberg, C. & Handy, M. R. (2000). Syntectonic melt pathways during simple shearing of a partially molten rock analogue (Norcamphor-Benzamide). *Journal of Geophysical Research* **105**, 3135–3149.

Rosenberg, C. L. & Handy, M. R. (2001). Mechanisms and orientation of melt segregation paths during pure shearing of a partially molten rock analog (norcamphor-benzamide). *Journal of Structural Geology* **23**, 1917–1932.

Sibson, R. H. (1977). Kinetic shear resistance, fluid pressures and radiation efficiency during seismic faulting. *Pure and Applied Geophysics* **115**, 387–400.

Smith, C. A., Sisson, V. B., Avé Lallemant, H. G. & Copeland, P. (1999). Two contrasting pressure–temperature–time paths in the Villa de Cura blueschist belt, Venezuela: Possible evidence for Late Cretaceous initiation of subduction in the Caribbean. *Geological Society of America Bulletin* **111**, 831–848.

Spry, A. H. (1969). The interpretation of the textures of peridotites, eclogites and granulites. *Special Publication, Geological Society of Australia* **2**, 307–321.

Tribuzio, R., Tiepolo, M. & Thirlwall, M. F. (2000). Origin of titanian pargasite in gabbroic rocks from the Northern Apennine ophiolites (Italy); insights into the late-magmatic evolution of a MOR-type intrusive sequence. *Earth and Planetary Science Letters* **176**, 281–293.

Tucholke, B. E., Fujioka, K., Ishihara, T., Hirth, G. & Kinoshita, M. (2001). Submersible study of an oceanic megamullion in the central North Atlantic. *Journal of Geophysical Research* **106**, 16145–16161.

Vannucci, R., Piccardo, G. B., Rivalenti, G., Zanetti, A., Rampone, E., Ottilini, L., Oberti, R., Mazzucchelli, M. & Bottazzi, P. (1995). Origin of LREE-depleted amphiboles in the subcontinental mantle. *Geochimica et Cosmochimica Acta* **59**, 1763–1771.

Villiger, S., Ulmer, P., Müntener, O. & Thompson, A. B. (2004). The liquid line of descent of anhydrous, mantle-derived, tholeiitic liquids by fractional and equilibrium crystallization; an experimental study at 1·0 GPa. *Journal of Petrology* **45**, 2369–2388.

Vissers, R. L. M., Drury, M. R., Hoogerduijn Strating, E. H. & Van der Wal, D. (1991). Shear zones in the upper mantle; a case study in an Alpine lherzolite massif. *Geology* **19**, 990–993.

Vissers, R. L. M., Drury, M. R., Hoogerduijn Strating, E. H., Spiers, C. J. & Van der Wal, D. (1995). Mantle shear zone and their effect on lithosphere strength during continental break-up. *Tectonophysics* **249**, 155–171.

Vissers, R. L. M., Drury, M. R., Newman, J. & Fliervoet, T. F. (1997). Mylonitic deformation in upper mantle peridotites of the North Pyrenean Zone (France): implications for strength and strain localization in the lithospere. *Tectonophysics* **279**, 303–325.

Warren, J. M. & Hirth, G. (2006). Grain size sensitive deformation mechanisms in naturally deformed peridotites. *Earth and Planetary Science Letters* **248**, 438–450.

Witt-Eickschen, G. & Seck, H. A. (1991). Solubility of Ca and Al in orthopyroxene from spinel peridotite; an improved version of an empirical geothermometer. *Contributions to Mineralogy and Petrology* **106**, 431–439.